CDF/ANAL/BOTTOM/CDFR/11044
Version 1.2
October 7, 2013

Measurement of D^0 meson production cross-section at low transverse momentum

Jeffrey A. Appel, Manuel Mussini[1], Diego Tonelli

Abstract

We report on a measurement of the D^0 meson production cross-section as a function of the D^0 transverse momentum in the range $1.5 < p_{\rm T}(D^0) < 14.5$ GeV/c. Hadronic $D^0 \to K^-\pi^+$ decays are reconstructed in the full CDF Run II data set collected with the zero bias and minimum bias triggers. Their event yields, subtracted by the component originated from b-hadron decays, are corrected for the effect of acceptances and efficiencies, derived from simulation, to determine the cross section. The results may provide useful information to understand heavy flavor hadroproduction at energy scales where predictions based on perturbative approaches are not possible.

Contents

[1]mussini@fnal.gov

1 Introduction and motivation

The early Run II CDF measurement of the prompt charm production cross section [1, 2] had a significant impact in the QCD community. It was the first TeV-scale measurement of charm production in hadron-hadron collisions in a scenario where large discrepancies were observed between measured heavy-flavor cross sections and NLO predictions. Nowadays, the predictions have been improved and calculations with the FONLL expansion [3] accommodate better the experimental data. However, the kinematic regime studied by that measurement was limited, since the cross section, differential in the D^0 transverse momentum, probed a minimum $p_{\rm T}$ of 5.5 GeV/c, because of the biases introduced by the Two Track Trigger (TTT) selection. Extending the measurement to lower transverse momenta would be extremely useful for the theory, providing additional experimental lever arm to refine the calculations in a regime where c-quark production occurs in nonperturbative conditions. The large amount of data collected during CDF Run II offers the chance to study the production of heavy-flavored mesons in the zero bias (ZB) and minimum bias (MB) samples. These samples are collected through minimal experimental biases, hence allowing to extend the transverse momentum range of the produced particles to the lowest values achievable at CDF II. The ZB and the MB triggers impose minimal and generic requests in order to reduce biases to the physics properties of the collected data, at the price of a reduced fraction of heavy-flavor events compared to the large light-quark background. However, in the full 10/fb sample of Run II data, the size of these minimally biased samples is such that a significant amount of charm decays may be present and allow reconstruction of visible exclusive signals. Recently, other measurements of charm production cross-section at low-p_T became available from the ALICE and LHCb experiments at the CERN LHC proton-proton collider. However, the present measurement maintains its uniqueness in terms of initial state ($p\bar{p}$) and center-of-mass energy, and supplements the LHC determinations.

This measurements builds upon the study of [4], where we reported the first attempt at reconstructing an exclusive charm signal in the minimum bias sample. We choose the $D^0 \to K^-\pi^+$ decay mode because of its simple topology (two-body decay with charged final state), its sizable branching fraction (Br($D^0 \to K^-\pi^+$) $\approx$ 3.9 %) and because the previous CDF measurement [1, 2] provides a useful reference in the fraction of kinematic regime that is common to both measurements.

The analysis is a standard cross-section measurement, differential in D^0 meson transverse momentum in the range $1.5 < p_T(D^0) < 14.5$ and $|y(D^0)| < 1$. First, candidate two-body decays are reconstructed in the ZB and MB samples with a loose set of standard selection requirements for track and vertex quality, without exploiting any kind of particle identification information. The charged kaon mass is arbitrarily assigned to the negatively-charged final-state particle and the charged pion mass to the positively-charged one to determine each candidate's two-body invariant mass. We take into account of the equal amount of misreconstructed charge-conjugate decays in

the yields determination. Then, a $p_T(D^0)$-specific multidimensional optimization of the selection criteria yields a more effective final selection able to isolate a visible charm signal down to $p_T \approx 1.5$ GeV/c. The $D^0 \to K^-\pi^+$event yields are determined by fitting the invariant $K\pi$ mass distribution and subtracting the component originated from b-hadron decays. This is derived from data, using auxiliary fits of the D^0 candidates' impact parameter distribution.
Geometric acceptance and reconstruction efficiencies derived from simulation are used to correct the raw yields, which are finally divided by the integrated luminosity of the sample to obtain the cross section.

2 Differential Cross Section

Equation 1 describes how the cross section is calculated in this analysis. The determination of each factor in the formula is described separately in a section of this note.

$$\left.\frac{d\sigma}{dp_{\rm T}}\right|_{|y|\leq 1} = \frac{\frac{1}{2}Y(p_{\rm T})f_{\rm D}(p_{\rm T})}{\Delta p_{\rm T}\mathcal{L}_{\rm TRIG}\varepsilon_{\rm TRIG}\varepsilon_{\rm REC}(p_{\rm T})Br(D^0 \to K\pi)} \tag{1}$$

- $Y(p_{\rm T})$ is the number of charm mesons in each $p_{\rm T}$ bin measured from a fit of the invariant $K^-\pi^+$ mass distribution. The factor of 1/2 is included because the fit determines both D^0 and $\bar{D}^0$ meson yields, while we report the cross section for D^0 mesons only. See Section 4.

- $f_{\rm D}(p_T)$ is the fraction of *direct* charm, that is the fraction of charm mesons produced directly in the proton-antiproton hard scatter, in that bin (prompt signal). See Section 5.

- $\Delta p_{\rm T}$ is the bin width.

- $\mathcal{L}_{\rm TRIG}$ is the trigger live luminosity. See Section 3.

- $\varepsilon_{\rm TRIG}$ is the efficiency associated with the trigger selection. See Section 6.

- $\varepsilon_{\rm REC}(p_{\rm T})$ is the efficiency associated with the reconstruction. It includes acceptance effects and accounts for the slope of the cross section within each bin. See Section 7.

- Br$(D^0 \to K\pi)$ is the decay branching ratio.

Because in general the average value of cross section in bin i, $\sigma_{\rm i}/\Delta p_{\rm T,i}$, differs from the value corresponding to the p_T value of the center of the bin, we report the differential cross section $d\sigma/dp_{\rm T}$ integrated over the width of each bin. We reweighted the cross section distribution used to generate the simulated signal to match the one observed.

3 $\mathcal{L}_{\mathrm{TRIG}}$ - The data samples

We use the samples collected by the `ZEROBIAS` (ZB) and the `MINBIAS` (MB) trigger paths over the course of the whole Run II Tevatron operations. Information on total event yields is summarized in Tables 1 and 2.

DSID	gcrs (ZB)	gmbs (MB)
cm	43 605 515	25 687 729
ah	20 658 162	12 334 739
ai	5 451 922	3 177 091
bi	23 992 815	16 439 018
bj	15 585 273	11 629 919
bk	11 122 054	8 902 794
ap	93 541 841	75 574 822
Sum	213 957 582	153 746 112
Total	367 703 694	

Table 1: *Total events in the sample divided by dataset ID (DSID).*

	gcrs (ZB)	gmbs (MB)
Sum	182 565 407	132 871 206
Total	315 432 920	
Overlap	409	

Table 2: *Events in the sample after the GRL selection.*

3.1 Zero Bias trigger

The `ZEROBIAS` trigger requirements are the following:

Level 1: any bunch crossing fires L1. Prescale factor = 1,000,003.

Level 2: no requests.

Level 3: no requests.

No information from any CDF II subdetector is used by this trigger to set its decision. The ZB trigger is designed to provide a genuine random sampling of the bunch crossing, independently of whether the crossing produced a hard scattering or not. Because of the L1 prescale factor, approximately 1.7 events per second are accepted.

3.2 Minimum Bias trigger

The `MINBIAS` requirements are the following:

Level 1: CLC signals coincidence. Prescale factor = 100,003.

Level 2: any event is automatically accepted by L2 within a rate limit = 3 Hz.

Level 3: any event is automatically accepted by L3 within a rate limit = 1 Hz.

The events collected by the MB trigger are enriched in inelastic collisions because at L1 a signal of at least 250 ADC counts is required in at least one of the East Cherenkov luminosity counters (CLC) in coincidence with an equivalent signal in the West CLC.

3.3 Event overlap

The two trigger selections operate at the same time during the data taking. Hence, the same event might be accepted by both triggers and be duplicated in the sample. If there were no prescales or rate limiters, the `MINBIAS` sample would be fully included in the `ZEROBIAS` sample. However, because of the prescales and rate limiters, the fraction of duplicated events is at the 10^{-6} level. Indeed, we find that 409 events out of more than 315×10^6 events are present in both samples. In what follows these events are used only once and the effect of the overlap on key variables (e.g. trigger luminosity) is completely negligible w.r.t. their uncertainties.

3.4 Good Run List and luminosity

We use the official QCD good run list (GRL) that contains only runs where SVX II and the COT were working properly. The small fraction of runs for which the database reports unreliable luminosity values are discarded. After these requests the ZB sample isreduced to $\sim$ 183 million events while the MB sample to $\sim$ 133 million events.
The raw integrated luminosity stored on the database is corrected for the usual 1.9% factors listed in Table 3 to derive the actual trigger luminosity of the sample $\mathcal{L}_{\rm TRIG}$ (= $\mathcal{L}_{\rm RAW} \cdot 1.019$).

	$\mathcal{L}_{\rm RAW}$	$\mathcal{L}_{\rm RAW} \cdot 1.019$
ZB	8.90	9.07
MB	6.83	6.96
Tot	15.73	16.03

Table 3: *Luminosity corrections for ZB, MB and total samples in* $(nb)^{-1}$.

3.5 Monte Carlo simulation

Simulated Monte Carlo samples are used in this analysis chiefly to evaluate the absolute reconstruction efficiency, derive mass templates for the yields fits, and derive the impact parameter distributions of charm mesons from b hadron decays used to separate the direct fraction. The simulated samples are generated using `BGENERATOR` with input y–p_{T}in the [-1.3; 1.3]×[0; 15] GeV/c range, derived from heavy flavor events filtered out of a Pythia-generated sample (see Figure 1) and use it to generate the samples with `BGENERATOR`. No trigger simulation or selection is performed on the generated samples.

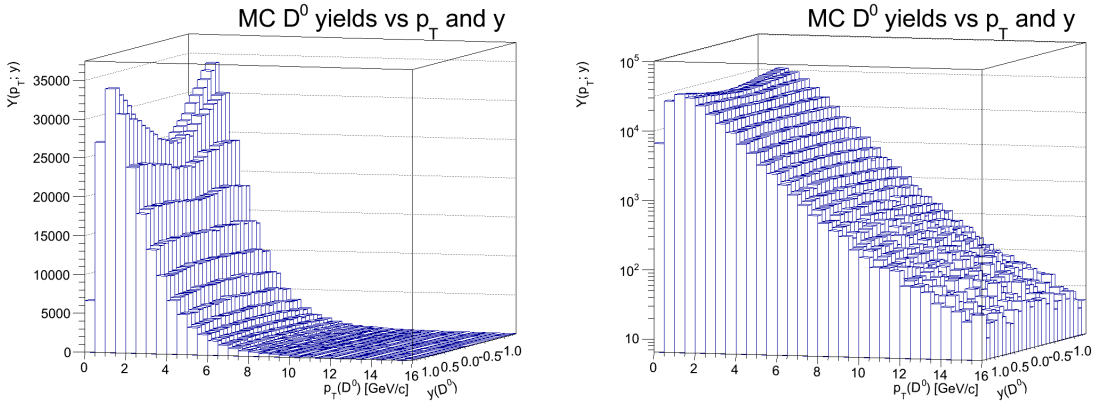

Figure 1: *y–$p_T$distribution used to generate the D^0 samples: linear (left) and log (right) scale.*

3.5.1 $D^0 \to K\pi$

We generate a sample of about 124 million D^0 and $\bar{D}^0$ mesons in equal proportions, forced to decay into the $K\pi$ final state. The simulation of the CDF II detector reproduces the changes in configurations observed across the actual operations. The events are distributed across the data-taking periods P0–P38, in proportions that approximate the integrated luminosity collected in each period. These samples are used to derive mass templates to be used in the yields fits.

Figure 2 shows the resulting invariant $K^-\pi^+$ mass distribution[2]. The plot shows a narrow peak centered at the known D^0 mass with a width of about 8 MeV/c^2 and a wider enhancement centered at the same mass but with a ten-times larger width. The narrow structure represents the charm signal obtained when the masses are correctly assigned to the charged particles, the broad enhancement is the result of misaligned masses.

Figure 3 shows the same candidates of Figure 2 but in a two-dimensional mass plot showing the $K^+\pi^-$mass in the vertical axis and the $K^-\pi^+$mass on the horizontal axis. hypothesis. Figure 2 is the projection of this plot on the horizontal axis.

[2]The candidate selection used to obtain this distribution will be discussed in Section 4.

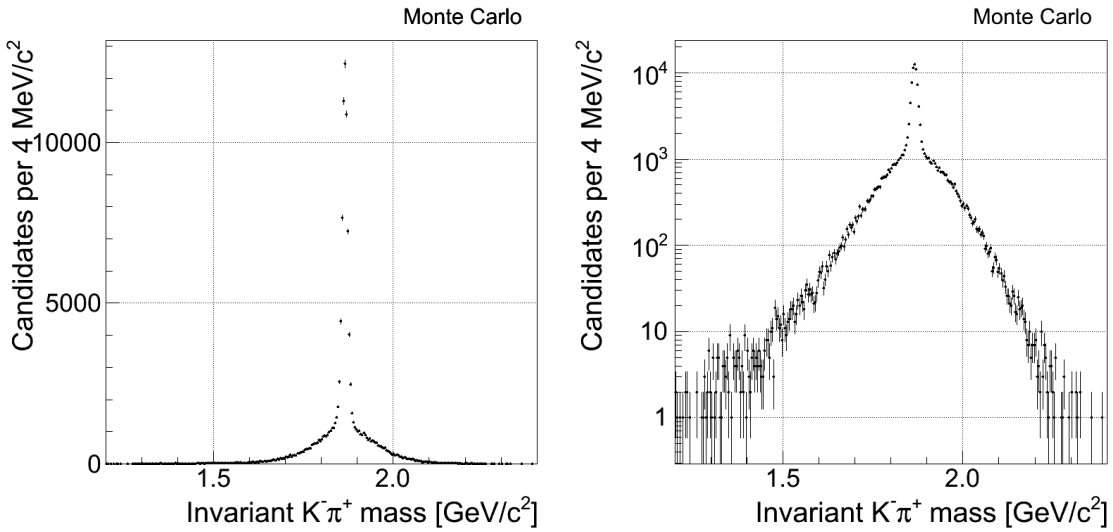

Figure 2: *Invariant $K^-\pi^+$mass of candidates reconstructed in the $D^0 \to K\pi$ MC sample: linear (left) and logarithmic scale (right).*

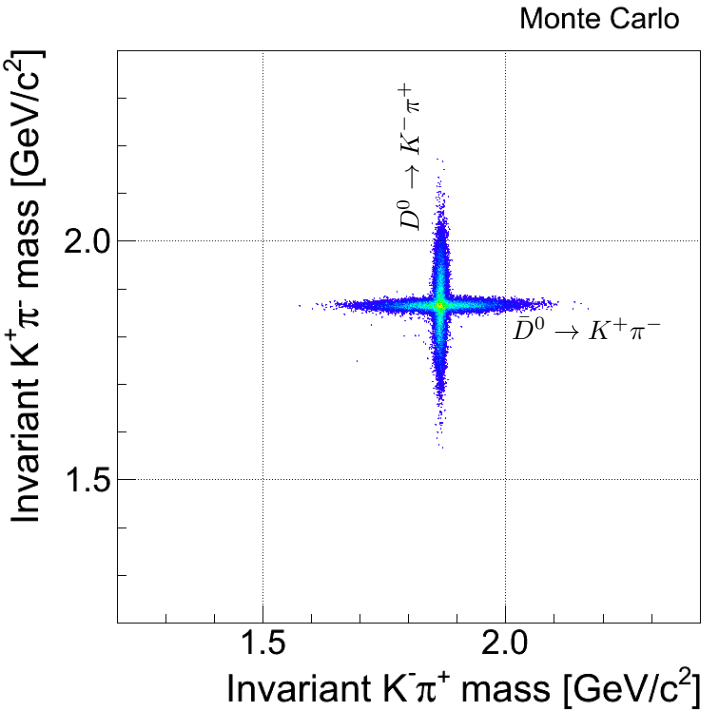

Figure 3: *2D invariant mass plot of candidates reconstructed in the $D^0 \to K\pi$ MC sample: $K^+\pi^-$ assignment in the y axis vs $K^-\pi^+$ assignment in the x axis.*

3.5.2 $B^{0,\pm} \to D^0 X$

We generated a sample of 37 million B^0 and 37 million $B^\pm$ decays forcing them to decay only into channels involving at least one D^0 in the final state. We forced the charm mesons to decay into $K\pi$ final states. This sample, discussed in Section 5, is used to extract the templates to assess the direct fraction of D^0.

4 Y - Signal yield

4.1 Reconstruction

Figure 4 illustrates the topology of a D^0 that decays into $K^-\pi^+$.

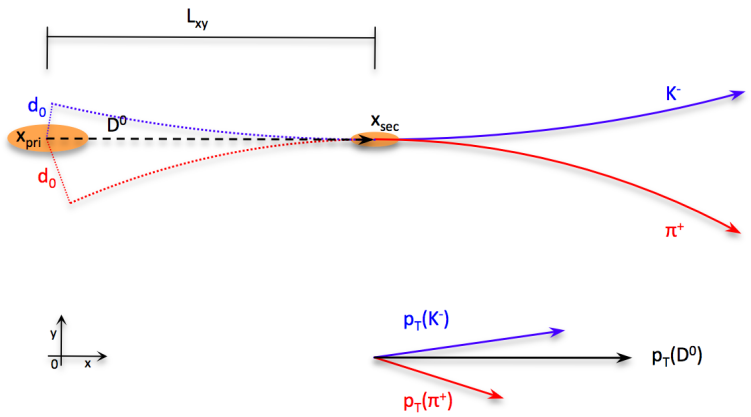

Figure 4: *Graphical representation of the topology of the $D^0 \to K^-\pi^+$ decay channel in the transverse plane.*

In each event, the D^0 candidates are reconstructed offline by combining all the possible pairs of tracks (with opposite curvature) into a kinematic fit looking for an intersection point displaced from the primary vertex. The charged kaon (pion) mass is arbitrarily assigned to the negative (positive) final state particle. In addition to the $D^0 \to K^-\pi^+$ Cabibbo favored (CF) channel, the $\bar{D}^0 \to K^+\pi^-$ doubly-Cabibbo-suppressed (DCS) channel contributes to the signal with the same final state, but its effect is negligible. Offline tracks are subject to the following baseline requirements:

- SVX II small angle stereo (SAS) hits ≥ 1 (out of 2);
- SVX II stereo (z) hits ≥ 2 (out of 3);
- SVX II axial (r-φ) hits ≥ 3 (out of 6);
- COT stereo hits ≥ 25 (out of 48);
- COT axial hits ≥ 25 (out of 48);

- $p_{\mathrm{T}}(\mathrm{TRK}) \geq 0.5$ GeV/c;
- $|\eta| \leq 1.2$;
- $0 \leq |d_0| \leq 0.1$ cm;

where η is the track's pseudorapidity and d_0 its impact parameter.

All possible pairs of good tracks are then required to meet the following criteria:

- $q_1 \cdot q_2 < 0$;
- $d_{0,1} \cdot d_{0,2} < 0$;
- $\Delta z_0(TRK) = |z_{0,1} - z_{0,2}| \leq 0.5$ cm;

with q_1 and q_2 the charges of the tracks.

Then each pair of tracks is fit looking for a possible common origin point displaced from the primary vertex using the CTVMFT package [8]. A D^0 candidate is selected if:

- $L_{\mathrm{xy}} \geq 0$ cm;
- $|y(D^0)| \leq 1$;
- $\chi^2 \leq 10$;

where $y(D^0)$ is the candidate's rapidity, L_{xy} its travelled path (in the transverse plane) before decaying and χ^2 is the global fit χ^2. Figure 5 shows the invariant $K^-\pi^+$ mass distribution for candidates selected with the base selection, as described above, integrating the candidates with $p_{\mathrm{T}}(D^0) \geq 1.5$ GeV/c.

The distribution shows a clear peak at the known D^0 mass. We expect that only a half of the $D^0 \to K\pi$ candidates are contained in the visible signal, while the other half (with misassigned masses for the outgoing particles) has a broader shape indistinguishable from the background.

4.2 $D^0 \to K^-\pi^+$ shapes

The event yield of signal events restricted to each transverse momentum range is determined by a fit to the invariant $K\pi$ mass distribution. The shapes used in this fit are obtained from simulation. We study the D^0 signal shape as a function of $p_{\mathrm{T}}(D^0)$using the simulated $D^0 \to K\pi$ sample described in Sec. 3.5.1. The mass line shape is parametrized through the probability density function (pdf) shown in Eq. (2).

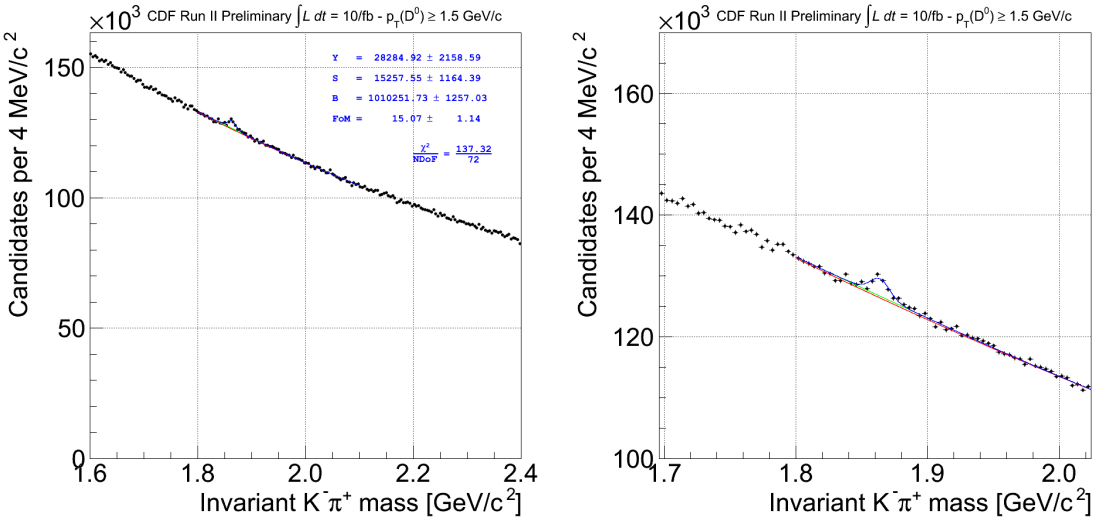

Figure 5: *Invariant $K^-\pi^+$ mass distribution of candidates that satisfy the base selection discussed in the text (zoom of the fit region on the right).*

$$pdf_{D^0}(m;\vec{\theta}_{D^0}) = f\ (g\ \mathscr{G}(m;m_{D^0}+\delta_1,\sigma_1) + (1-g)\mathscr{G}(m;m_{D^0}+\delta_2,\sigma_2)) + \\ +\ (1-f)\mathscr{T}(m;b,c,m_{D^0}+\delta_1) \tag{2}$$

where $\mathscr{G}(m;\mu,\sigma)$ is the usual normalized Gaussian distribution, and

$$\mathscr{T}(m;b,c,\mu) = \frac{1}{K}e^{b(m-\mu)}\cdot \mathrm{Erfc}(c(m-\mu)) \tag{3}$$

is an empiric function including the normalization factor K and the error function

$$\mathrm{Erfc}(x) = 1-\mathrm{Erf}(x) = \frac{2}{\sqrt{\pi}}\int_x^{+\infty} e^{-t^2}dt \tag{4}$$

The pdf is a sum of two Gaussians and a low-mass tail, which accounts for soft photon emission; the parameter f is the relative fraction of the double Gaussian contribution w.r.t. the total, g is the relative fraction of the narrow Gaussian core labeled with the index *1* w.r.t. the sum of the two Gaussians, $\sigma_{1(2)}$ is the width of the Gaussian *1* (*2*) and $\delta_{1(2)}$ is a mass shift from the known m_{D^0} mass due to the asymmetry induced by the soft photon emission. The parameters $\vec{\theta}_{D^0} = \{f, g, \sigma_1, \sigma_2, \delta_1, \delta_2, b, c\}$ are extracted by fitting the simulated invariant $K^-\pi^+$ mass for signal-only canddiates. Figures 6 and 7 show the result of the parametrization of the D^0 signal in each bin of $p_{\mathrm{T}}(D^0)$ in linear and logarithmic scale, respectively. The small discrepancies in the tail model

are well below the precision we need[3]. The shapes obtained show that the D^0 signal width does not depend significantly on p_T in the range of interest.

4.3 $\bar{D}^0 \to K^+\pi^-$ shapes

We've similarly studied the $\bar{D}^0$ signal shape as a function of $p_{\rm T}(\bar{D}^0)$. We used again the $D^0 \to K\pi$ MC sample described in Section 3.5.1. The mass line shape of the $\bar{D}^0$ decay is parameterized through the same pdf used for the D^0 but the vector of parameters $\vec{\theta}_{\bar{D}^0}$ is now extracted by fitting the simulated invariant $K^-\pi^+$ mass distribution when a $\bar{D}^0$ is generated, as shown in Equation 5.

$$pdf_{\bar{D}^0}(m;\vec{\theta}_{\bar{D}^0}) = f\ (g\ \mathscr{G}(m; m_{D^0}+\delta_1, \sigma_1) + (1-g)\ \mathscr{G}(m; m_{D^0}+\delta_2, \sigma_2)) + \\ +\ (1-f)\cdot \mathscr{T}(m; b, c, m_{D^0}+\delta_1) \tag{5}$$

Figure 8 shows the result of the parameterization for the $\bar{D}^0$ signal for each bin of $p_{\rm T}(\bar{D}^0)$. Figure 9 shows the same plots but in logarithmic scale on the y axis to highlight the presence of the radiative tail. The small discrepancies in the tails are well below the precision we need. Unlike the D^0 signal, the $\bar{D}^0$ fits show an evident dependence on the $p_{\rm T}(\bar{D}^0)$: the width of the distribution increases when the momentum grows.

4.4 Background

4.4.1 Combinatorial component

The shape of background candidates formed by pairs of random tracks that accidentally meet the selection's cannot be reliably determined from the mass sidebands, since these are also populated by a significant fraction of signal decays where the mass assignment is swapped. Hence, we study the shape of the combinatorial background by reconstructing candidates in which the charges of the final state particles are required to be the same. This allows keeping the same selection and the secondary vertex fitting procedures used for signal reconstruction, while ensuring that no real $D^0 \to K\pi$contribute, due to the same-charge requirement. A decreasing exponential shape provides an accurate approximation of the combinatorial background mass as shown in Figure 10. While we used an arbitrary selection of the candidates for this example plot, similar level of agreement is observed in any configuration of the selection. The combinatorial background parametrization is shown in Eq. (6).

$$pdf_{\rm B}(m;\vec{\theta}_{\rm B}) = \frac{1}{K} e^{-m\cdot q} \tag{6}$$

[3]The value N_f/N_H reported on the plots represents the ratio between the integral of the fit function and the entries in the plot.

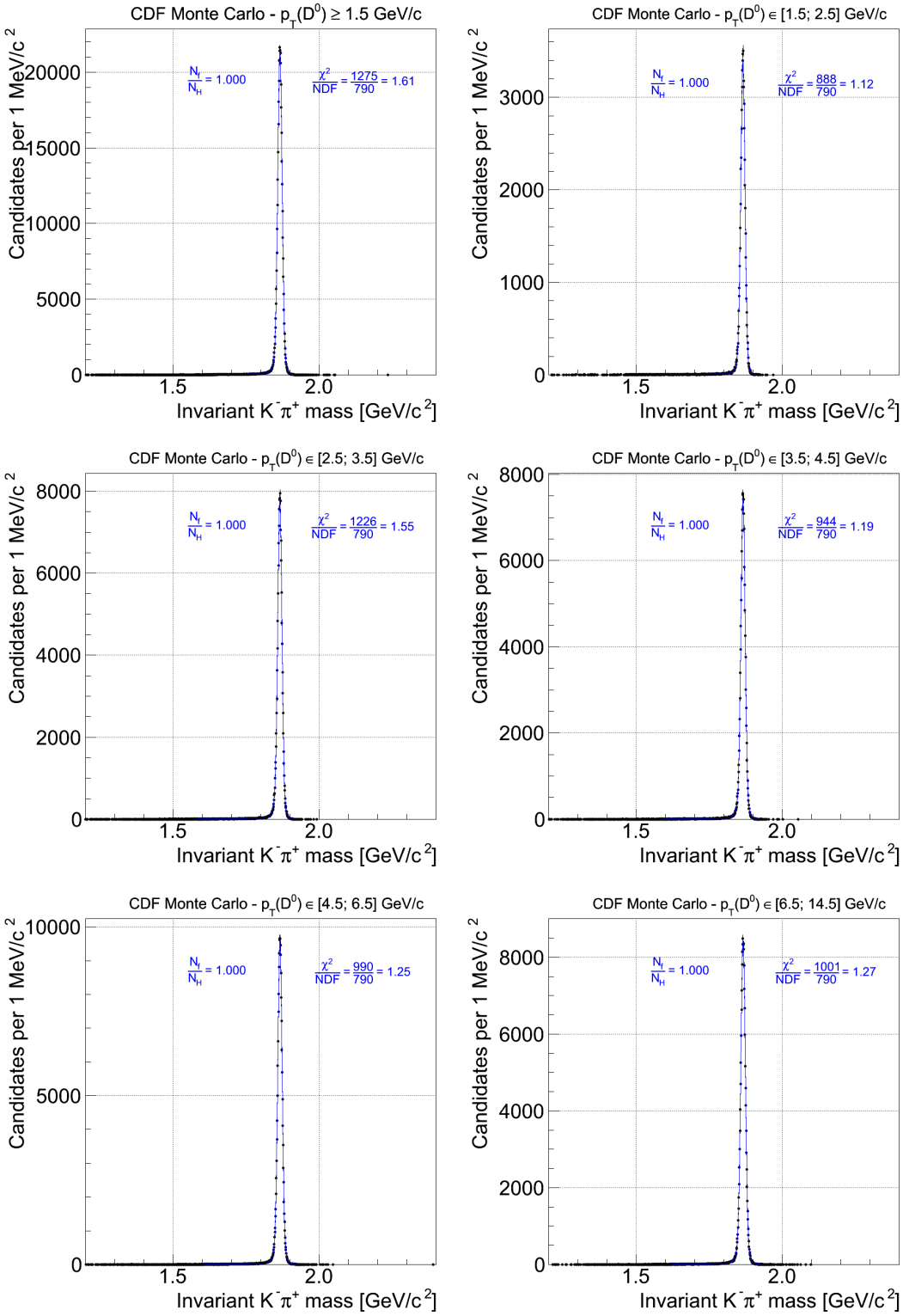

Figure 6: *Invariant $K^-\pi^+$ mass distribution of MC events for the D^0 reconstruction for each bin of $p_T(D^0)$ and for $p_T(D^0) \geq 1.5$ GeV/c.*

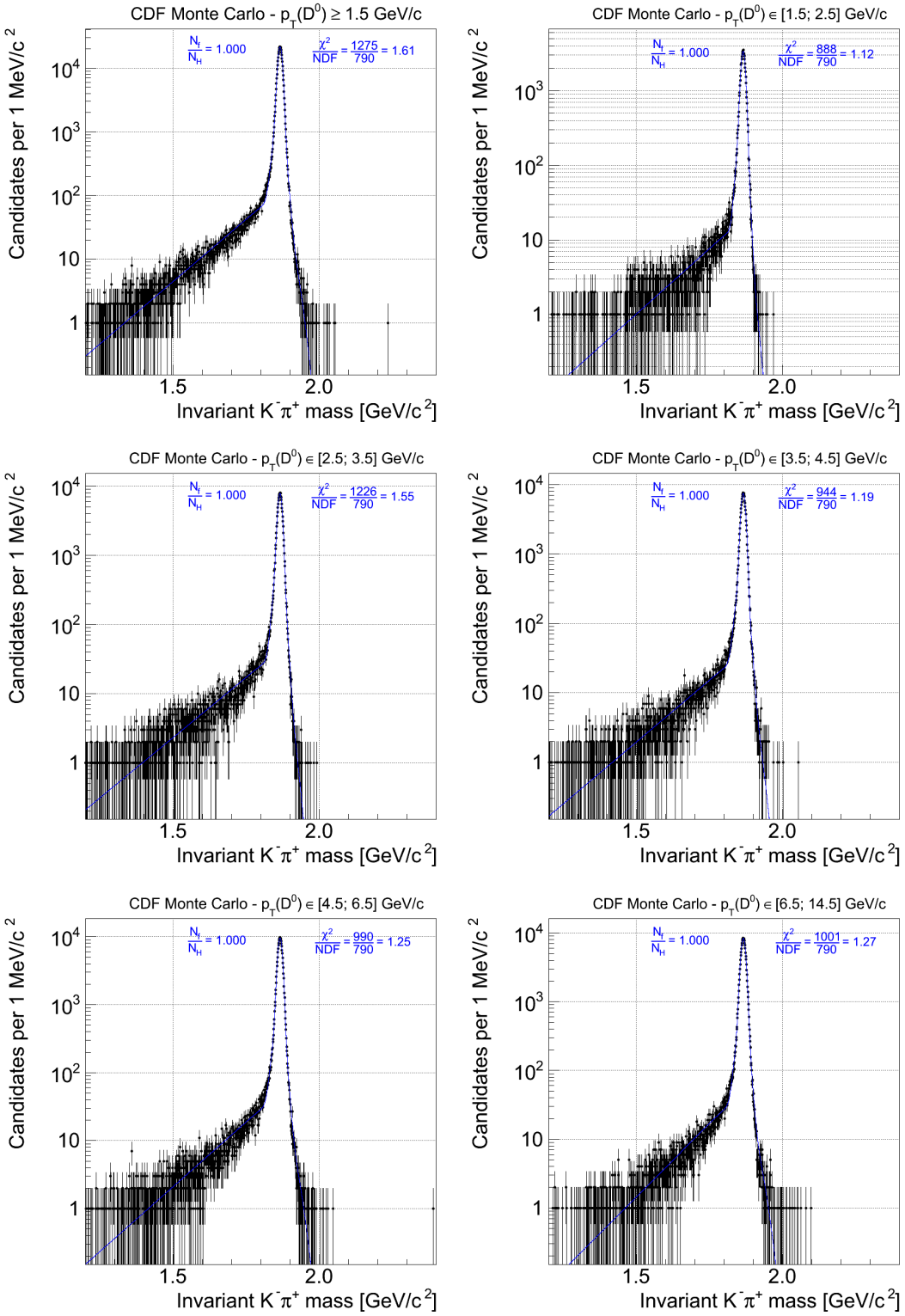

Figure 7: *Invariant $K^-\pi^+$ mass distribution of MC events for the D^0 reconstruction for each bin of $p_T(D^0)$ and for $p_T(D^0) \geq 1.5$ GeV/c.*

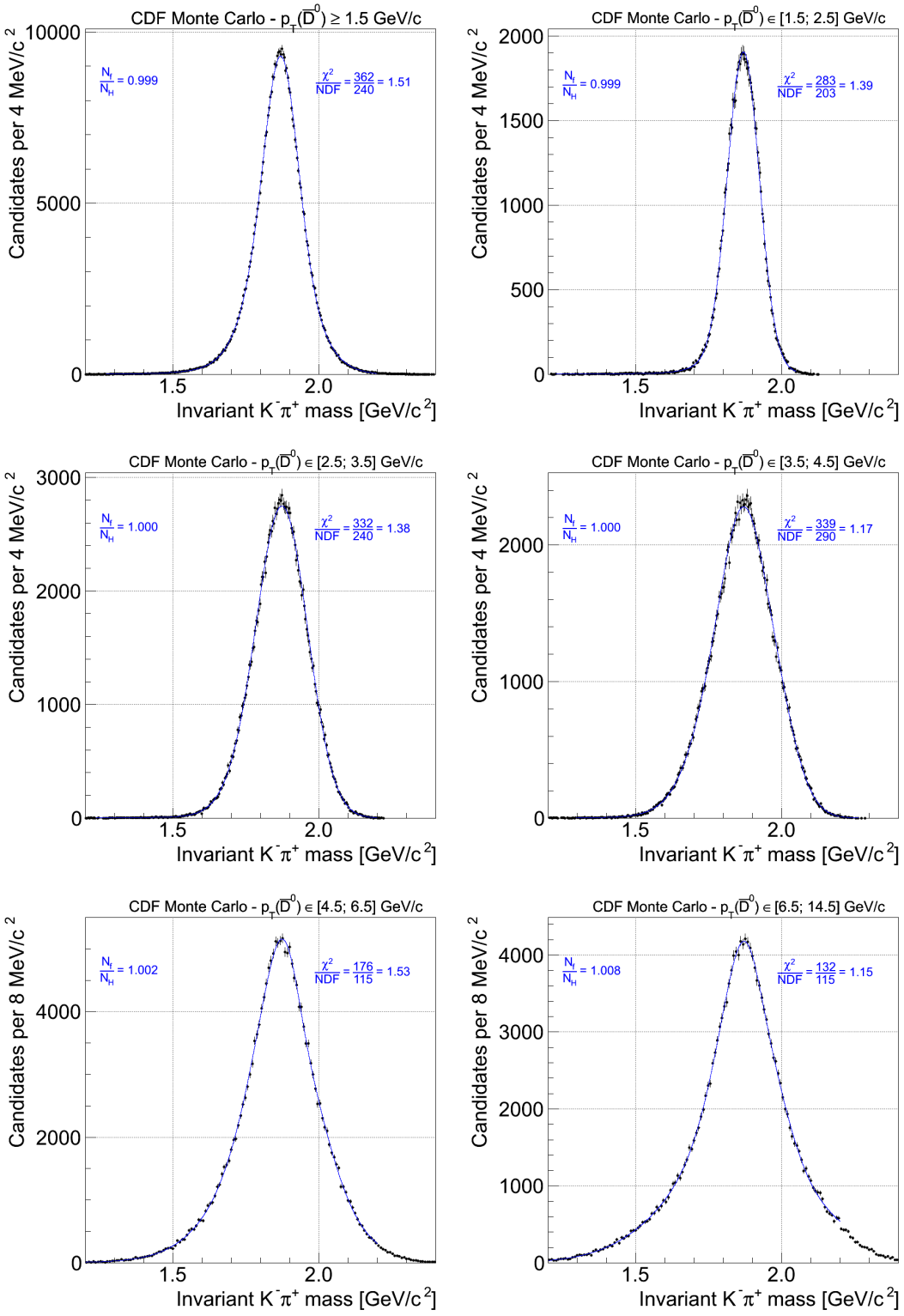

Figure 8: *Invariant $K^-\pi^+$ mass distribution of MC events for the $\bar{D}^0$ reconstruction for each bin of $p_T(\bar{D}^0)$ and for $p_T(\bar{D}^0) \geq 1.5$ GeV/c.*

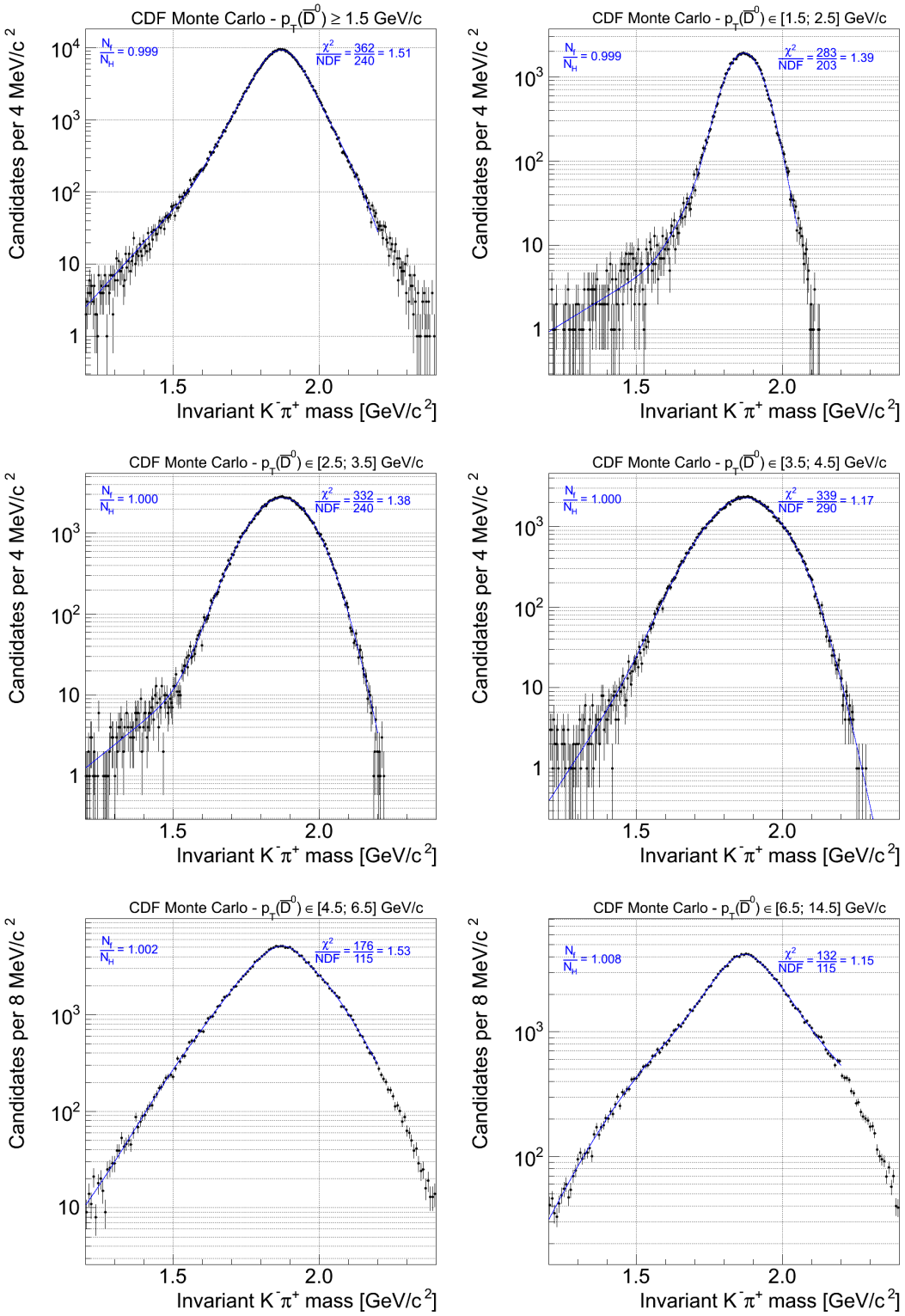

Figure 9: *Invariant $K^-\pi^+$ mass distribution of MC events for the $\bar{D}^0$ reconstruction for each bin of $p_T(\bar{D}^0)$ and for $p_T(\bar{D}^0) \geq 1.5$ GeV/c.*

where K is an appropriate normalization and $\vec{\theta}_{\rm B} = \{q\}$.

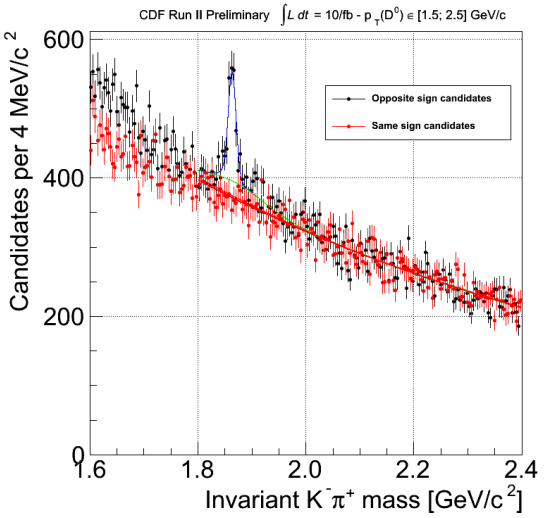

Figure 10: *Invariant $K^{\pm}\pi^{\pm}$ mass distribution of data events for same sign candidates in the first $p_T(D^0)$ bin used in the analysis. Also the opposite sign candidates are plotted to show that the two fits for the background (red lines) are compatible. The SS distribution is scaled by a + 5 %.*

4.4.2 Background from misreconstructed $D^0 \to X$ decays

A number of other D^0 decays can contribute to the signal region [15], Figure 11 shows the two-dimensional invariant mass plot for a data sample collected using the TTT, whose leading various component can be identified using simulation. Figure 12 shows these components in a projection onto the $K^+\pi^-$ axis. This allows identifying the region $1.8 < K^+\pi^- < 2.4$ GeV/c^2, where $D^0 \to X$ contributions are negligible. Hard-to-model multibody backgrounds are kinematically excluded from this region, which only suffers from a small $D^0 \to \pi^-\pi^+$ tail, which is expected to be negligible in the yield fits.

4.5 $K^-\pi^+$ mass fit

We now have all the ingredients needed to fit the invariant $K^-\pi^+$ distributions to measure the yield of the D^0 signal. All fits use the function shown in Eq. (7). We perform a likelihood fit to the binned $K^-\pi^+$ mass distribution in the range $1.8 < m < 2.4$ GeV/c^2

$$F(Y;B;q) = Y\ (f\ pdf_{D^0} + (1-f)\ pdf_{\bar{D}^0}) + B\ pdf_{\rm B}(q) \tag{7}$$

where

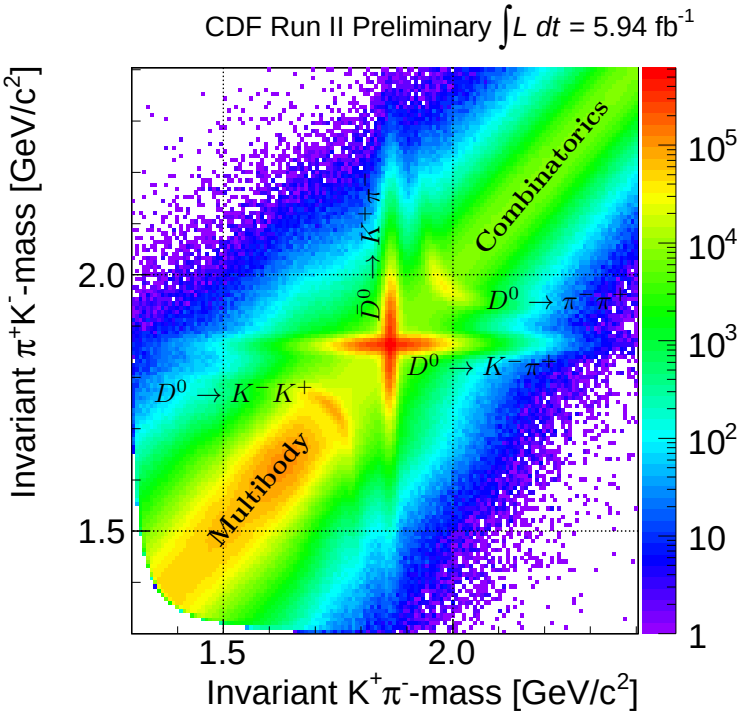

Figure 11: *2D invariant mass plot of candidates reconstructed in the $D^0 \to X$ MC sample: $K^+\pi^-$ assignment in the y axis vs $K^-\pi^+$ assignment in the x axis.*

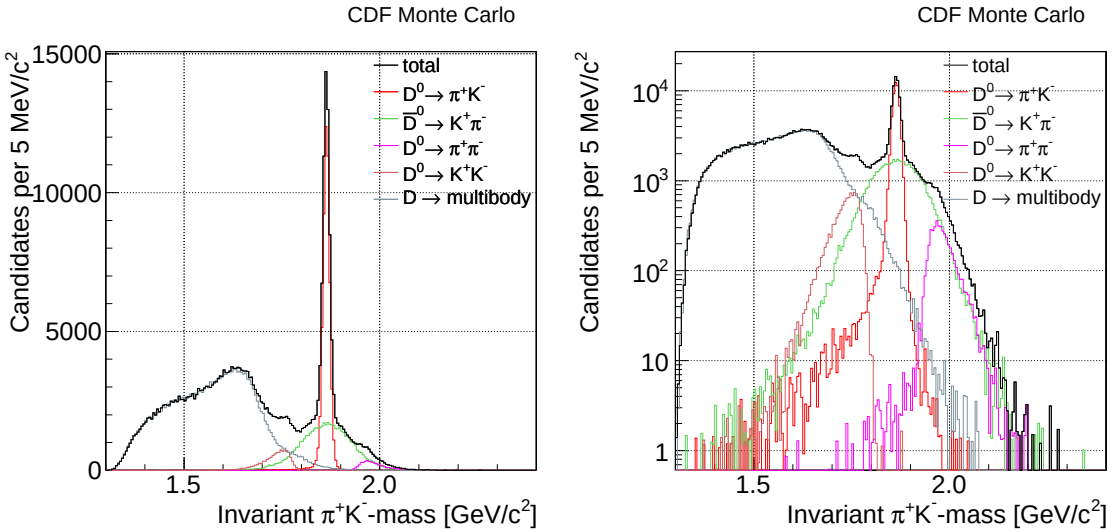

Figure 12: *Invariant $K^-\pi^+$ mass of candidates reconstructed in the $D^0 \to X$ MC sample.*

- Y, B and q are free parameters.
- the D^0 and $\bar{D}^0$ pdfs are fixed as described in the previous sections.

- The fraction, f, of the D^0 signal w.r.t. the sum of D^0 and $\bar{D}^0$ is fixed to 0.5 because we assume charge invariance in the QCD production and identical reconstruction efficiencies.

4.6 Selection optimization

Before proceeding to fit the signal yield in each transverse momentum bins, we use the fit to obtain an optimized offline selection to minimize the final statistical uncertainty on the cross-section measurement. We optimize the candidate selection separately for each bin of $p_{\rm T}$by maximizing the figure-of-merit $f(S;B) = S/\sqrt{S+B}$, where S and B are the signal and background yields, respectively, within 16 MeV/c^2 from the D^0 peak , as a function on various thresholds in a suited set of selection requirements. After exploring various combinations of discriminating variables, we choose the following five most discriminating variables to perform the optimization: $p_{\rm T}$(TRK), $\Delta z_0(TRK)$, $d_0(TRK)$, $\chi(D^0)$ and $L_{\rm xy}(D^0)$. For each variable ten different thresholds are tested, as defined in Table 4.6.

Variable	Range	Step
$p_{\rm T}$(TRK)	0.5 – 1.4 GeV/c	0.1 GeV/c
$\Delta z_0(TRK)$	0.5 – 0.05 cm	0.05 cm
$d_0(TRK)$	0 – 180 μm	20 μm
$\chi(D^0)$	10 – 1	1
$L_{\rm xy}(D^0)$	0 – 360 μm	40 μm

Table 4: *Cuts tested for the 5 variables of the optimization.*

Each selection is identified through a five-digits code, where each digit represent the step for each variable; e.g., the base selection used to obtain the plot in Figure 5 is coded as 00000.

We follow [10] to perform an unbiased optimization directly on data. The main steps of the procedure are as follows:

- Consider the data sample $\mathcal{S}$ in which an optimization of the selection is required.
- $\mathcal{S}$ is subdivided into two mutually exclusive subsamples, $\mathcal{A}$ and $\mathcal{B}$, using a random criterion.
- The same optimization procedure is applied independently on both subsamples:
    1. A criterion is defined to identify the signal events $S_i^{\mathcal{A}}$ and the background events $B_i^{\mathcal{A}}$ surviving the i-th configuration of the selection cuts in sample $\mathcal{A}$ (e.g., performing a fit of the candidates invariant mass distribution).

2. The chosen figure of merit, $f(S_i^{\mathcal{A}}, B_i^{\mathcal{A}})$, is maximized over the space of configurations for the selection requirements (e.g., all combinations of cuts).
3. The configuration of cuts corresponding to the maximum of f defines the set of cuts optimized in sample $\mathcal{A}$.
4. Steps 3 and 4 are repeated in sample $\mathcal{B}$ to obtain the set of cuts optimized in sample $\mathcal{B}$, different in general from the one obtained in sample $\mathcal{A}$.

- The final sample used for the analysis is obtained by applying to the subsample $\mathcal{B}$ the cuts optimized in sample $\mathcal{A}$ and viceversa.

Figure 13 visually describes the procedure.

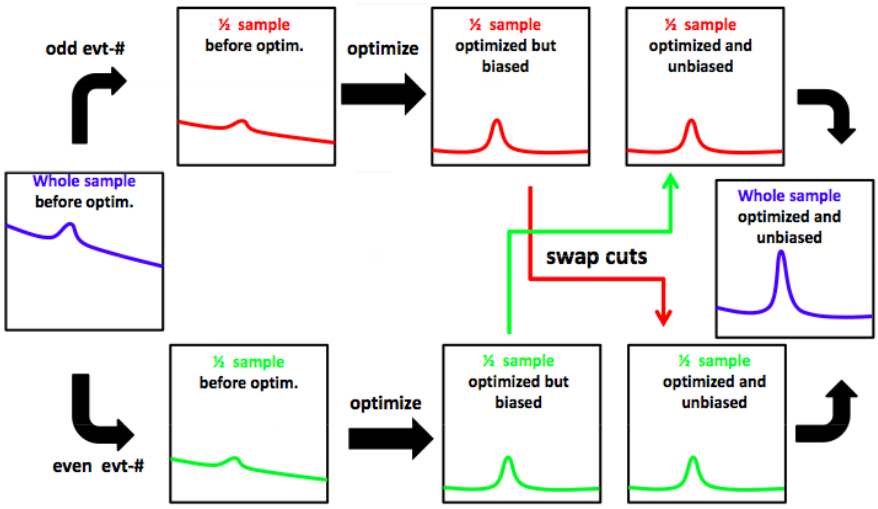

Figure 13: *Scheme of the data based selection optimization procedure.*

To apply this optimization method in our analysis we define the following criteria:

- The two statistically independent subsamples of approximately the same size are obtained using the event number, splitting the sample between even and odd events.

- Signal and background are obtained through a likelihood fit of the invariant $K^-\pi^+$ mass plot as described in Section 4.5.

- Two sets of cuts are obtained based on the event number, an "even" optimal configuration and an "odd" optimal one. They are swapped, applying the *even* optimal configuration to the *odd* subsample and the *odd* optimal configuration to the *even* sample.

For each subsample the optimization algorithm evaluates the figure of merit for each selection configuration, thus, probing the whole five-dimensional space of requirements. Figures 14 and 15 are an example of the optimization procedure for the candidates with $p_{\mathrm{T}}(D^0) \geq 1.5$ GeV/c. The plots at the top of Figure 14 show the two optimal selections for even (left) and odd (right) events; the bottom plots are the result of the crossing of the selections. Figure 15, finally, shows the union of the optimized subsamples (the two on the bottom of Figure 15) and Table 5 summarizes the results of the optimization for the even and odd samples.

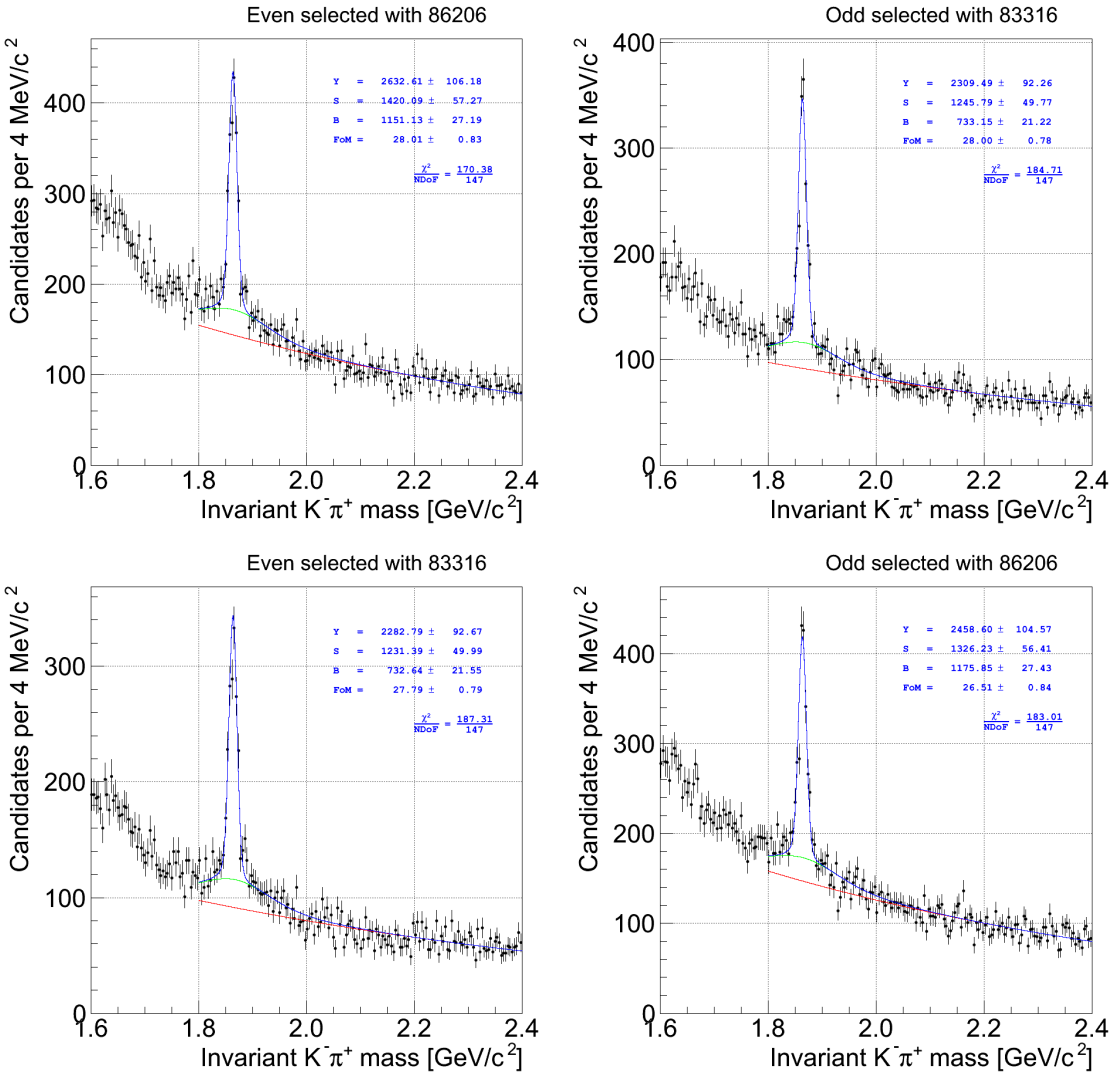

Figure 14: *Invariant $K^-\pi^+$ mass plots of the selections that maximizes the FoM (top), for even (left) and odd (right) events, and for the crossed selections (bottom). Candidates with $p_T(D^0) \geq 1.5$ GeV/c are used.*

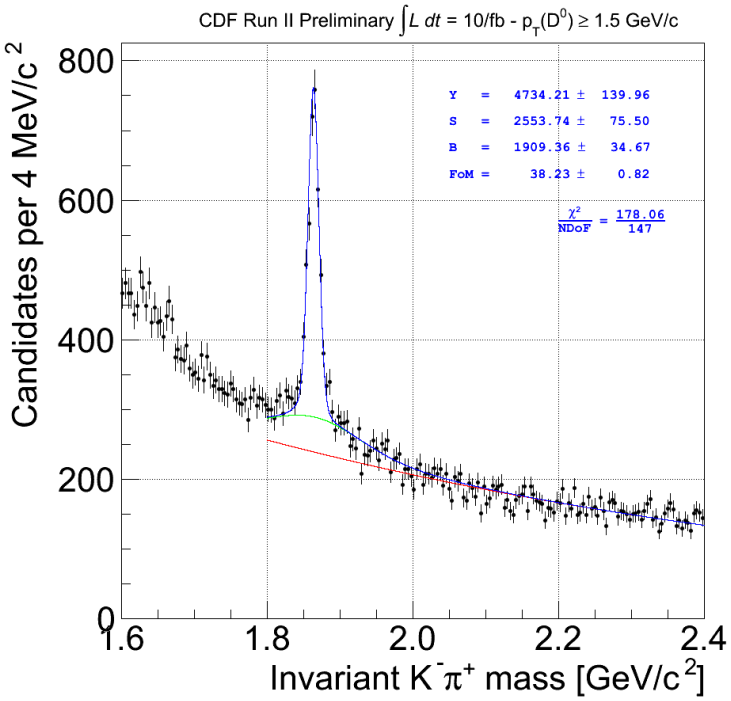

Figure 15: *Invariant $K^-\pi^+$ mass plots of the resummed optimized subsamples for candidates with $p_T(D^0) \geq 1.5$ GeV/c.*

p_T [GeV/c]	E \O	Code	p_T(TRK) $\geq$	$\Delta z_0 \leq$	$\lvert d_0(\text{TRK})\rvert \geq$	$\chi^2 \leq$	$L_{xy} \geq$	FoM
1.5 – 2.5	Even	44540	0.9	0.3	100	6	0	10.45
	Odd	14776	0.6	0.3	140	3	240	12.25
2.5 – 3.5	Even	33400	0.8	0.35	80	10	0	16.21
	Odd	13456	0.6	0.35	80	5	240	16.87
3.5 – 4.5	Even	26217	0.7	0.2	40	9	280	16.18
	Odd	40306	0.9	0.5	60	10	240	16.64
4.5 – 6.5	Even	10129	0.6	0.5	20	8	360	17.98
	Odd	40227	0.9	0.5	40	8	280	17.42
6.5 – 14.5	Even	42008	0.9	0.4	0	10	320	15.99
	Odd	44007	0.9	0.3	0	10	280	13.99

Table 5: *Selections that optimize the FoM for the even and odd samples.*

4.7 Yields as a function of $p_T(D^0)$

Figure 16 shows the results of the fits of the signal yield on data for each bin of $p_T(D^0)$ after the optimization procedure. The plot on the bottom right graphically summarizes the results, also reported in Table 6.

$p_{\rm T}$ [GeV/c]	$Y = D^0 + \bar{D}^0$
1.5 – 2.5	1537 ± 124 (8.1 %)
2.5 – 3.5	2361 ± 125 (5.3 %)
3.5 – 4.5	1662 ± 88 (5.3 %)
4.5 – 6.5	1697 ± 82 (4.8 %)
6.5 – 14.5	1399 ± 73 (5.2 %)

Table 6: *Signal yields (D^0 + $\bar{D}^0$) and statistical errors as a function of $p_T(D^0)$.*

5 $f_{\rm D}(p_T)$ - Direct fraction

5.1 B meson feed-down

Secondary D^0 and $\bar{D}^0$ decays produced in decays of B meson contribute to the signal sample. The direct fraction of D^0 mesons that are promptly produced in the $p\bar{p}$ interactions is determined by exploiting the difference in the $d_0(D^0)$ distributions between direct and secondary D^0 mesons. Because of the B lifetime, secondary D^0 appear as originating from a space-point displaced from the beam. Hence, the $d_0(D^0)$ distribution has a larger width with respect to the distribution from direct D^0 mesons. For each bin of $p_{\rm T}(D^0)$, the invariant mass of the candidates is fitted as a function of their $d_0(D^0)$ value. Then, the resulting event yields are plotted as a function of the impact parameter, and fit with a linear combination of impact parameter templates for prompt and for secondary mesons, as extracted from simulation.

5.2 Direct shape

The simulated $D^0 \to K\pi$ sample is used to parametrize the $d_0(D^0)$ distribution of the direct component in each $p_{\rm T}(D^0)$ bin using the linear combination of three Gaussian functions

$$pdf_{\rm DIR}(d_0;\vec{\theta}_{\rm DIR}) = f\ \mathscr{G}(d_0;d_{0,1},\sigma_1) + g\ \mathscr{G}(d_0;d_{0,2},\sigma_2) + (1-f-g)\ \mathscr{G}(d_0;d_{0,3},\sigma_3) \quad (8)$$

in which f (g) is the relative fraction of the Gaussian labeled with the index *1* (*2*) w.r.t. the sum of the three Gaussians and $\sigma_{1(2,3)}$ is the width of the Gaussian *1* (*2*, *3*). The parameters $\vec{\theta}_{\rm DIR} = \{f, g, \sigma_1, \sigma_2, \sigma_3, d_{0,1}, d_{0,2}, , d_{0,3}\}$ are extracted by fitting the impact parameter distribution of simulated direct mesons. Figures 17 and 18 show the result of the parametrization for each $p_{\rm T}(D^0)$ bin in linear and logarithmic scale, respectively. The small discrepancies in the tails are well below the needed precision.. The width of $d_0(D^0)$ decreases as the momentum grows.

5.3 Secondary shape

Similarly, we parametrize the $d_0(D^0)$ distribution as a function of $p_{\rm T}(D^0)$ for the secondary component using the simulated $B^{0,\pm} \to D^0 X$samples and the same Gaussian expansion used for the direct component:

$$pdf_{\rm SEC}(d_0;\vec{\theta}_{\rm SEC}) = f \cdot \mathscr{G}(d_0; d_{0,1}, \sigma_1) + g \cdot \mathscr{G}(d_0; d_{0,2}, \sigma_2) + (1 - f - g) \cdot \mathscr{G}(d_0; d_{0,3}, \sigma_3) \quad (9)$$

Figures 19 and 20 show the result of the parametrization for the $d_0(D^0)$ for each bin of $p_{\rm T}(D^0)$ in linear and logarithmic scale, respectively. The small discrepancies in the tails are well below the precision we need. As for the direct component, the shapes obtained show that the $d_0(D^0)$ width decreases when the momentum grows.

5.4 Direct fraction fit

We now have all the ingredients needed to fit the $d_0(D^0)$ distributions to measure the direct fraction of D^0 mesons in our signal. We perform a fit to the binned impact parameter distributions, using the following function

$$F(Y; f_{\rm D}) = Y \cdot (f_{\rm D} \cdot pdf_{\rm DIR} + (1 - f_{\rm D}) \cdot pdf_{\rm SEC}) \quad (10)$$

where Y and $f_{\rm D}$ are the only free parameters and direct and secondary pdfs are fixed. Figure 21 visually describe the described procedure to measure the direct fraction.

5.5 Direct fraction as a function of $p_{\rm T}(D^0)$

Figure 22 shows the results of the fits of the $d_0(D^0)$ distribution on data for each bin of $p_{\rm T}(D^0)$ (Figure 23 shows the same plots but in logarithmic scale); the plot on the bottom right of the Figures graphically summarizes the results and they are also reported in Table 7.

$p_{\rm T}$ [GeV/c]	$f_{\rm D}$
1.5 – 2.5	0.658 ± 0.021 (3.2 %)
2.5 – 3.5	0.678 ± 0.017 (2.5 %)
3.5 – 4.5	0.826 ± 0.017 (2.1 %)
4.5 – 6.5	0.863 ± 0.016 (1.9 %)
6.5 – 14.5	0.840 ± 0.022 (2.6 %)

Table 7: *D^0 direct fraction (f_D) and statistical errors as a function of $p_T(D^0)$.*

6 $\varepsilon_{\mathbf{TRIG}}$ - Trigger efficiency

6.1 $\varepsilon_{\mathbf{ZB}}$

The only possible source of inefficiency for the ZB trigger is the dead time occurred through the three-level trigger chain. However, each trigger path's luminosity is automatically corrected by this non-operating time. Hence, the value stored in the luminosity database does not need to be corrected because of data cellection inefficiency and the value for the ZB trigger $\varepsilon_{\mathrm{ZB}}$ is 1 [11].

6.2 $\varepsilon_{\mathbf{MB}}$

The MB trigger efficiency may depend on crossing and event conditions as instantaneous luminosity ($\mathcal{L}_{\mathrm{INST}}$), number of charged particles in the event, maximum track p_{T}, overall E_{T}, pile-up, etc. This is reflected in an increasing efficiency as a function of these variables because the probability of a matching signal in both East and West CLC increases. Several studies to understand these dependencies were performed during Run II [12, 13, 14]. Because the ZB trigger path is 100 % efficient, we use data to evaluate the efficiency correction for the MB sample. In fact, each CDF event reports the trigger status for each trigger present in the trigger table. Thus we check if a particular ZB event was also triggered by the `MINBIAS` trigger at L1 and perform a combined fit of the invariant $K^-\pi^+$ mass distributions for ZB events that fired or not the MB trigger. Figure 24 shows the result of the fit for candidates with $p_{\mathrm{T}}(D^0) \geq 1.5$ GeV/c. We performed the fit using the same function used for the other invariant $K^-\pi^+$ mass plots (see Equation 7) but setting the slope of the exponential function used for the background as a common parameter. We can then evaluate the efficiency of the MB trigger, $\varepsilon_{\mathrm{MB}}$, as stated in Equations 11 and 12:

$$\varepsilon_{\mathrm{MB}} = \frac{Y_{\mathrm{ZB\ \&\ MB}}}{Y_{\mathrm{ZB\ \&\ MB}} + Y_{\mathrm{ZB\ no\ MB}}} \tag{11}$$

$$\sigma_{\varepsilon_{\mathrm{MB}}} = \sqrt{\frac{\varepsilon_{\mathrm{MB}} \cdot (1 - \varepsilon_{\mathrm{MB}})}{Y_{\mathrm{ZB\ \&\ MB}} + Y_{\mathrm{ZB\ no\ MB}}}} \tag{12}$$

where $Y_{\mathrm{ZB\ \&\ MB}}$ and $Y_{\mathrm{ZB\ no\ MB}}$ are the fitted signal yields in ZB events that triggered the MB L1 bit or not. In our case we hit a limit case because we obtain $\varepsilon_{\mathrm{MB}} = 1$ and $\sigma_{\varepsilon_{\mathrm{MB}}} = 0$. To be conservative, we've decided to assess it in the worst case scenario: $Y_{\mathrm{ZB\ no\ MB}} = 2 \cdot \sigma_{+Y_{\mathrm{ZB\ no\ MB}}} = 8.34$. Equations 13 and 14 show the values we obtain

$$\varepsilon_{\mathrm{MB}} = \frac{1494.03}{1494.03 + 8.34} = 0.9944 \tag{13}$$

$$\sigma_{\varepsilon_{\mathrm{MB}}} = \sqrt{\frac{0.9944 \cdot (1 - 0.9944)}{1494.03 + 8.34}} = 0.0019 \tag{14}$$

This result confirms that the two subsamples (ZB and MB) can be safely added because any uncertainty is negligible with respect to the final 5–10% uncertainties we expect. In principle the MB trigger might be sensitive to the effects listed above also in case of events with a D^0 candidate. Since the efficiency is so high, it turns out not to be sensitive to them. We assume $\varepsilon_{\rm MB}$ to be 1 and treat the uncertainty as a systematic effect.[4].

7 $\varepsilon_{\rm REC}(p_{\rm T})$ - Reconstruction efficiency

To evaluate the reconstruction efficiency as a function of $p_{\rm T}(D^0)$ we use simulated $D^0 \to K\pi$ decays. We determine the efficiency as the fraction of D^0 and $\bar{D}^0$ candidates reconstructed after the full analysis with respect to the candidates generated in $|y| \leq 1$

$$\varepsilon_{\rm REC}(p_{\rm T}(D^0)) = \frac{N_{\rm REC}(p_{\rm T}(D^0))\big|_{\rm CUTS}}{N_{\rm GEN}(p_{\rm T}(D^0))\big|_{|y|\leq 1}} \tag{15}$$

Table 8 summarizes this ratio in our range of interest and Figure 25 shows the global trend.

$p_{\rm T}(D^0)$ [GeV/c]	$\varepsilon_{\rm REC}(p_{\rm T})$ [%]
1.5 – 2.5	0.5894 ± 0.0013
2.5 – 3.5	2.140 ± 0.003
3.5 – 4.5	3.680 ± 0.005
4.5 – 6.5	5.918 ± 0.007
6.5 – 14.5	12.455 ± 0.016

Table 8: *Reconstruction efficiency as a function of* $p_T(D^0)$.

This definition of $\varepsilon_{\rm REC}(p_{\rm T})$ represents a global reconstruction efficiency for our candidates. It takes into account several corrections introduced by the detector response, the reconstruction process and our selection:

- detector geometrical acceptance and response to the passage of particles;
- tracking efficiency in finding the charged particle's passage;
- efficiency and acceptance corrections introduced by our selection of the candidates;
- slope of the cross section used to generate the candidates within a bin.

[4]The ZB sample represents about the 42 % of the total; this reduces the effect of the MB trigger inefficiency to less than the 1 per mille.

The last point in the list assures that the value we will plot in each bin of the cross section distribution represents the integral of the cross section within each bin taking into account the slope of the distribution within that bin, as we discussed in Section 2.

8 Systematic uncertainties

8.1 Luminosity

As we discussed in Section 3.4 the measured trigger luminosity is obtained through the extrapolation of the total $p\bar{p}$ cross section from the measured value at $\sqrt{s} = 1.8$ TeV during the Run I; the systematic uncertainty associated to this extrapolation is assessed in [7] to be $\sigma^{\rm SYS}_{\mathcal{L}_{\rm TRIG}} = 5.8$ %.

8.2 Yield

Section 4.5 describes how we fit the invariant $K^-\pi^+$ mass plot. Each pdf used in the fit could be a possible source of systematic uncertainty: D^0, $\bar{D}^0$ and background.

To assess the possible variations to the final results due to a mismodeling of the D^0 and the $\bar{D}^0$ shapes, we've repeated the fits of the yields varying the parameters of the shapesone-at-a-time by $\pm\ 1\sigma$ of their values (as obtained from the fits described in Sections 4.2 and 4.3). The maximum variations, $\Delta Y_{\rm SIG}$, from the measured values are taken as systematic uncertainties.

For the combinatorial background, instead, we've repeated the fits using a second order polynomial function instead of the exponential one. The variations, $\Delta Y_{\rm BKG}$, from the measured values are taken as systematic uncertainties.

Another possible source of systematic uncertainty is the assumption that the ratio D^0:$\bar{D}^0$ is 1:1; we know from [15] that our choice is wrong at the per mille level. We can neglect this contribution.

Table 9 summarizes the numbers obtained for $\Delta Y_{\rm SIG}$ and $\Delta Y_{\rm BKG}$; $\sigma^{\rm SYS}_Y$ is the sum in quadrature of the two contributions.

$p_{\rm T}$ [GeV/c]	$\Delta Y_{\rm SIG}$	$\Delta Y_{\rm BKG}$	$\sigma^{\rm SYS}_Y$
1.5 – 2.5	0.1 %	2.3 %	2.3 %
2.5 – 3.5	0.4 %	2.9 %	2.9 %
3.5 – 4.5	0.5 %	2.2 %	2.3 %
4.5 – 6.5	0.8 %	2.5 %	2.6 %
6.5 – 14.5	0.4 %	0.4 %	0.6 %

Table 9: *Systematic uncertainties related to the yield measurement.*

8.3 Direct fraction

Section 5.4 describes how we fit for the direct fraction of D^0. Possible sources of systematic uncertainty are the mismodeling of direct and secondary shapes and the step width used to scan the $d_0(D^0)$. The fit is highly sensitive to the statistics of the plots and the tails of the distributions.

To assess the possible variations to the final results due to a mismodeling of the direct and the secondary components, we've repeated the fits of the direct fraction varying the parameters of the shapes by $\pm$ 1σ of their values (as obtained from the fits described in Sections 5.2 and 5.3). The maximum variations, $\Delta f_{\rm D}^{\rm SHAPE}$, from the measured values are taken as systematic uncertainties.

We repeated the fit using a different step width to scan the $d_0(D^0)$: 20 μm instead of 15 μm. The variations from the measured values are taken as systematic uncertainties. Table 10 summarizes the numbers obtained for $\Delta f_{\rm D}^{\rm SHAPE}$ and $\Delta f_{\rm D}^{\rm BIN}$; $\sigma_{f_{\rm D}}^{\rm SYS}$ is the sum in quadrature of the two contributions.

$p_{\rm T}$ [GeV/c]	$\Delta f_{\rm D}^{\rm SHAPE}$	$\Delta f_{\rm D}^{\rm BIN}$	$\sigma_{f_{\rm D}}^{\rm SYS}$
1.5 – 2.5	0.6 %	0.6 %	0.8 %
2.5 – 3.5	1.3 %	1.0 %	1.6 %
3.5 – 4.5	1.9 %	0.6 %	2.0 %
4.5 – 6.5	0.8 %	2.4 %	2.5 %
6.5 – 14.5	2.9 %	2.2 %	3.6 %

Table 10: *Systematic uncertainties related to the direct fraction measurement.*

8.4 Trigger efficiency

As described in Section 6.2 we measured the efficiency of the `MINBIAS` trigger to be (99.44 $\pm$ 0.19) %; we've assumed it to be 1 when summing the ZB and the MB subsample in the analysis and we treat the 0.19 % as a systematic uncertainty on this assumption. Because the MB sample is the 43 % of the total, the final effect on the measurement is $\sigma_{\varepsilon_{\rm TRIG}}^{\rm SYS} = 0.08$ %.

8.5 Reconstruction efficiency

Section 7 describes how we assess the reconstruction efficiency. To test the stability of the simulation, the $D^0 \to K^-\pi^+$ MC sample described in Section 3.5.1 has been generated mimicking all the 39 data taking periods. We've split it into 3 subsamples ([P0; P12], [P13; P25] and [P26;P38]) and reassessed the efficiencies for each one; the maximum variations, $\Delta\varepsilon_{\rm TIME}^{\rm SYS}$, from the measured values are taken as systematic uncertainties.

Also the reweighting procedure we described in the same Section introduces a systematic uncertainty. We assessed it varying the parameters of the function we use to

fit the cross section shape by $\pm\ 1\sigma$. The maximum variations, $\Delta\varepsilon^{\rm SYS}_{\rm REWEIGHT}$, from the measured values are taken as systematic uncertainties.
Table 11 summarizes the numbers obtained for $\Delta\varepsilon^{\rm SYS}_{\rm TIME}$ and $\Delta\varepsilon^{\rm SYS}_{\rm REWEIGHT}$; $\sigma^{\rm SYS}_{\varepsilon_{\rm REC}}$ is the sum in quadrature of the two contributions.

$p_{\rm T}$ [GeV/c]	$\Delta\varepsilon^{\rm SYS}_{\rm TIME}$	$\Delta\varepsilon^{\rm SYS}_{\rm REWEIGHT}$	$\sigma^{\rm SYS}_{\varepsilon_{\rm REC}}$
1.5 – 2.5	3.8 %	0.7 %	3.9 %
2.5 – 3.5	3.9 %	0.3 %	3.9 %
3.5 – 4.5	5.2 %	0.3 %	5.2 %
4.5 – 6.5	5.7 %	0.6 %	5.7 %
6.5 – 14.5	5.2 %	2.5 %	5.8 %

Table 11: *Systematic uncertainties related to the reconstruction efficiency measurement.*

8.6 Total systematic uncertainties

Table 12 summarizes the systematic uncertainties described in the previous sections; the last column is the sum in quadrature of all the contributions.

$p_{\rm T}$ [GeV/c]	$\sigma^{\rm SYS}_{\mathcal{L}_{\rm TRIG}}$	$\sigma^{\rm SYS}_{Y}$	$\sigma^{\rm SYS}_{f_{\rm D}}$	$\sigma^{\rm SYS}_{\varepsilon_{\rm TRIG}}$	$\sigma^{\rm SYS}_{\varepsilon_{\rm REC}}$	$\sigma^{\rm SYS}_{\rm TOT}$
1.5 – 2.5	5.8 %	2.3 %	0.8 %	0.08 %	3.9 %	7.4 %
2.5 – 3.5	5.8 %	2.9 %	1.6 %	0.08 %	3.9 %	7.7 %
3.5 – 4.5	5.8 %	2.3 %	2.0 %	0.08 %	5.2 %	8.4 %
4.5 – 6.5	5.8 %	2.6 %	2.5 %	0.08 %	5.7 %	8.9 %
6.5 – 14.5	5.8 %	0.6 %	3.6 %	0.08 %	5.8 %	9.0 %

Table 12: *Systematic uncertainties summary and final total values.*

9 Differential cross section

We can now put together all the ingredients needed in Equation 1 and evaluate the measured production cross section for each bin of $p_{\rm T}(D^0)$. Figure 26 shows the result of our measurement and Table 13 summarizes the value obtained in each bin.
We've compared our result with the previous CDF published measure [1] in Figure 27. A direct comparison in the plots is not possible because of the different bin widths used in the two measurements. Instead of fitting the two slopes, we've compared both of them with a FONLL prediction [3] as shown in Figure 28.

p_{T} [GeV/c]	$\frac{d\sigma}{dp_{\mathrm{T}}}$	$\pm$	stat	$\pm$	sys
1.5 – 2.5	137,413	$\pm$	12,049 (8.8 %)	$\pm$	10,169 (7.4 %)
2.5 – 3.5	59,925	$\pm$	3,575 (6.0 %)	$\pm$	4,614 (7.7 %)
3.5 – 4.5	29,882	$\pm$	1,752 (5.9 %)	$\pm$	2,510 (8.4 %)
4.5 – 6.5	9,906	$\pm$	527 (5.3 %)	$\pm$	882 (8.9 %)
6.5 – 14.5	945	$\pm$	57 (6.0 %)	$\pm$	85 (9.0 %)

Table 13: *Measured D^0 production cross section as a function of $p_T(D^0)$.*

10 Conclusions

In this note we've presented a study of the production of D^0 mesons (through one of its two-body decay channels, $D^0 \to K\pi$) using data collected by the `ZEROBIAS` and the `MINBIAS` triggers. We've measured the differential production cross section as a function of the transverse momentum down to $p_{\mathrm{T}} = 1.5$ GeV/c. This work presents the first measurement of the differential production cross section of this charmed meson to very low $p_{\mathrm{T}}(D^0)$ values at TeV collider energies.

The importance and uniqueness of this measurement has to be highlighted because even if new-generation accelerators, like the LHC, will be able to probe the same p_{T} range, their experimental conditions will not reproduce (at least for several decades from now) Tevatron ones both in terms of initial state ($p\bar{p}$) and center of mass energy ($\sqrt{s} = 1.96$ TeV).

Our result is in agreement with the published CDF II measurement [1] in the overlapping region. This gives us the complete p_{T} spectum of the D^0 production from $p_{\mathrm{T}}(D^0) = 1.5$ GeV/c to $p_{\mathrm{T}}(D^0) = 20$ GeV/c.

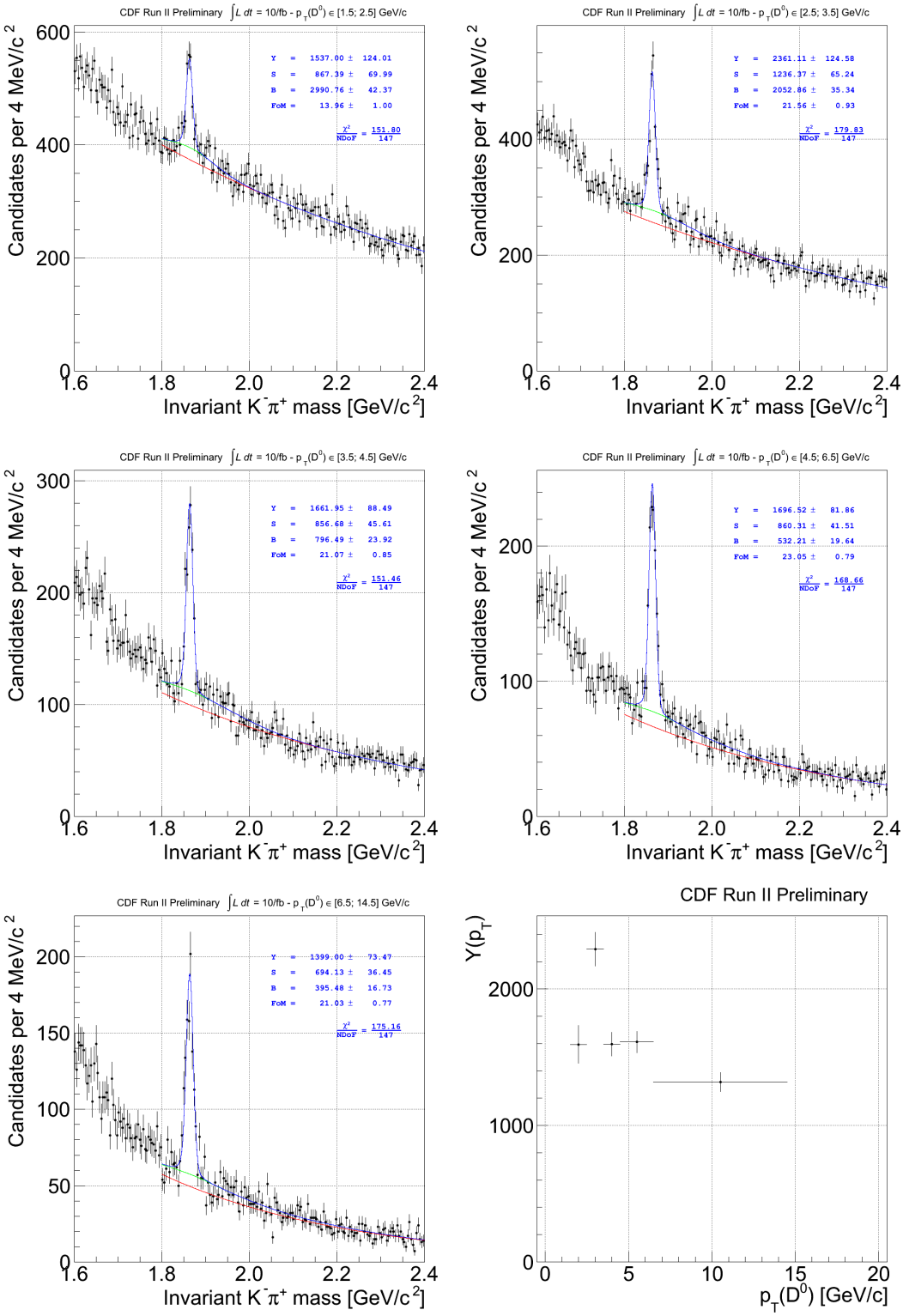

Figure 16: *Signal yields* $(D^0 + \bar{D}^0)$ *for each bin of* $p_T(D^0)$ *and as a function of* $p_T(D^0)$.

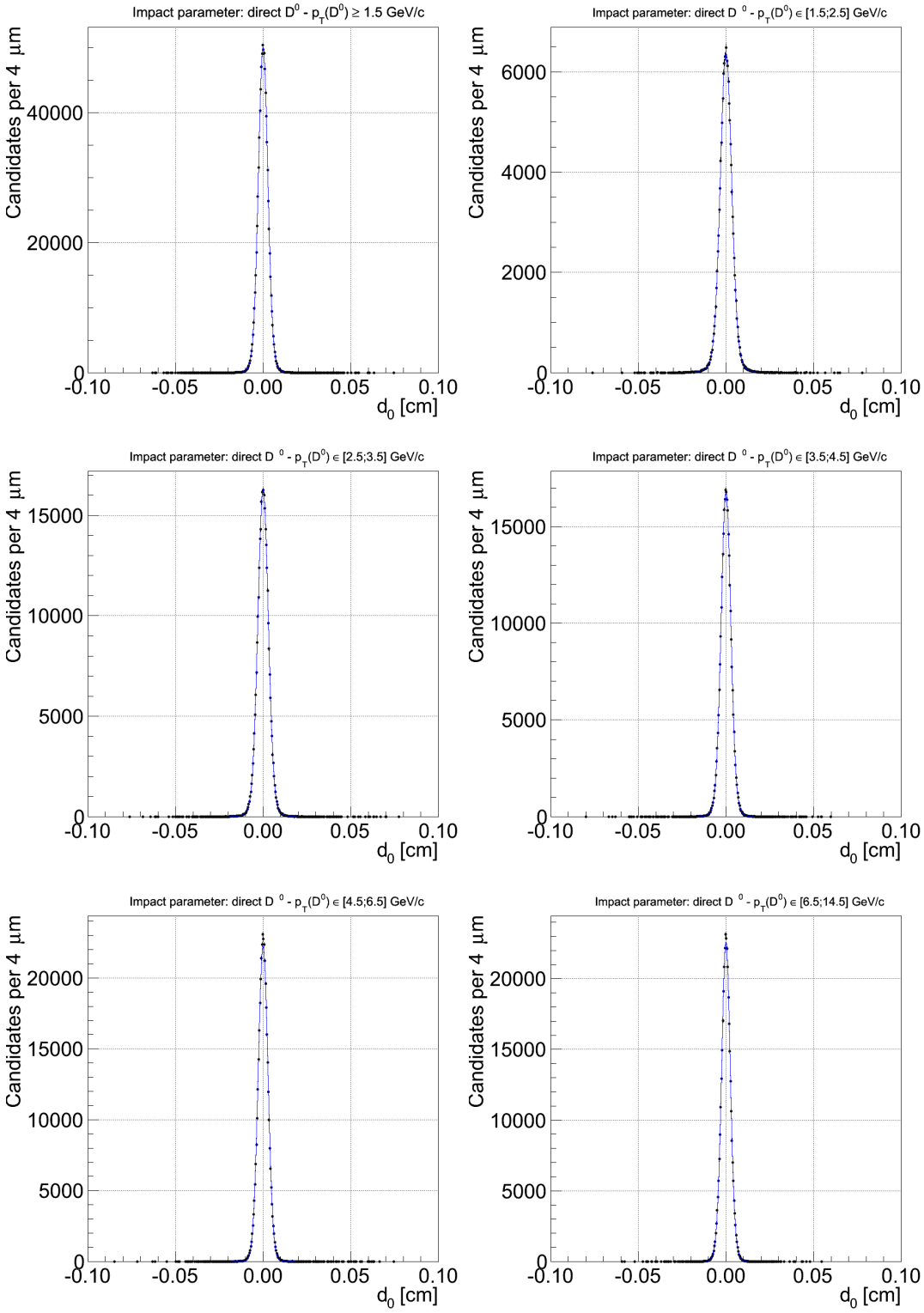

Figure 17: *$d_0(D^0)$distribution of MC events for the direct D^0 component for each bin of $p_T(D^0)$ and for $p_T(D^0) \geq 1.5$ GeV/c.*

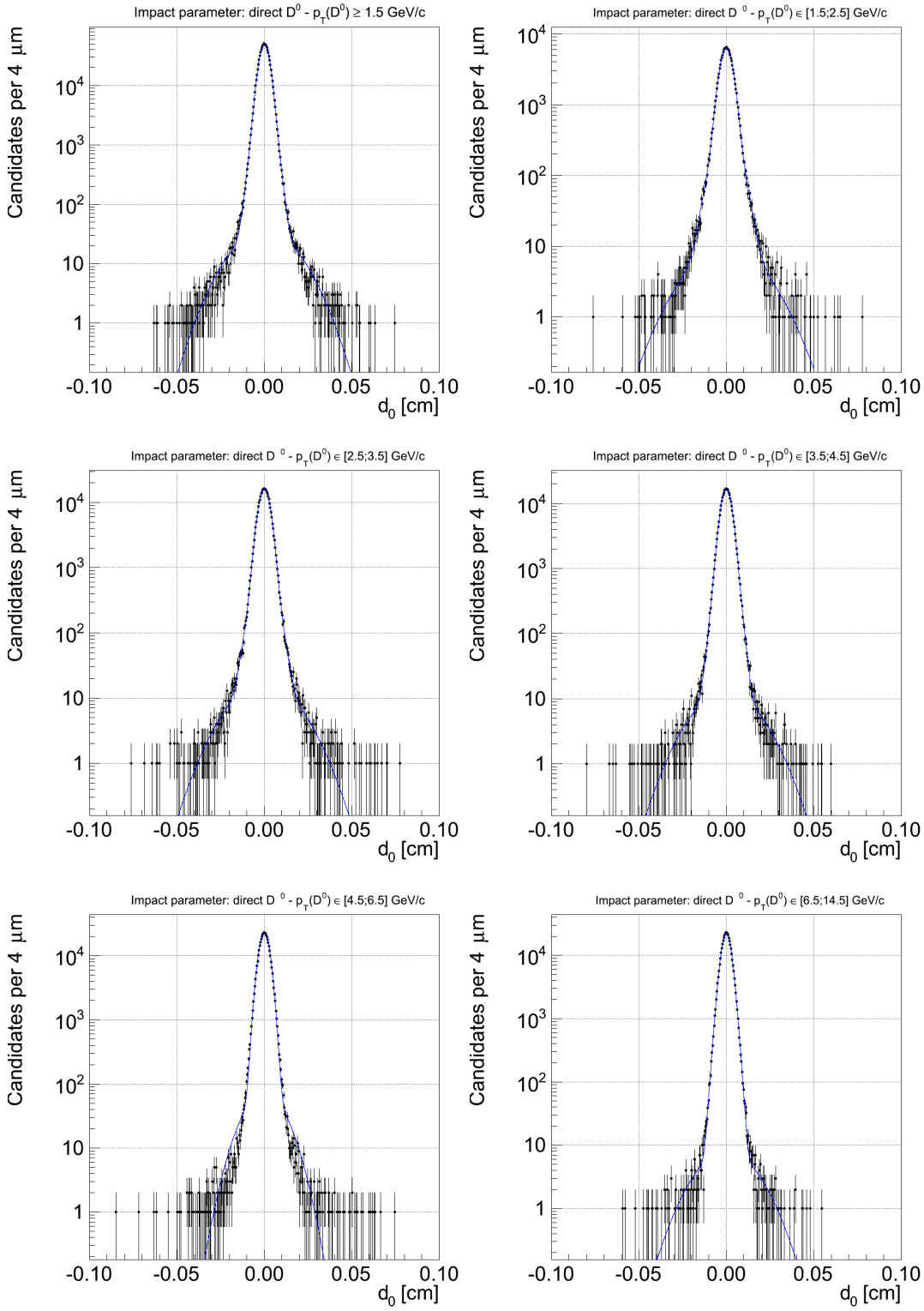

Figure 18: *$d_0(D^0)$distribution of MC events for the direct D^0 component for each bin of $p_T(D^0)$ and for $p_T(D^0) \geq 1.5$ GeV/c.*

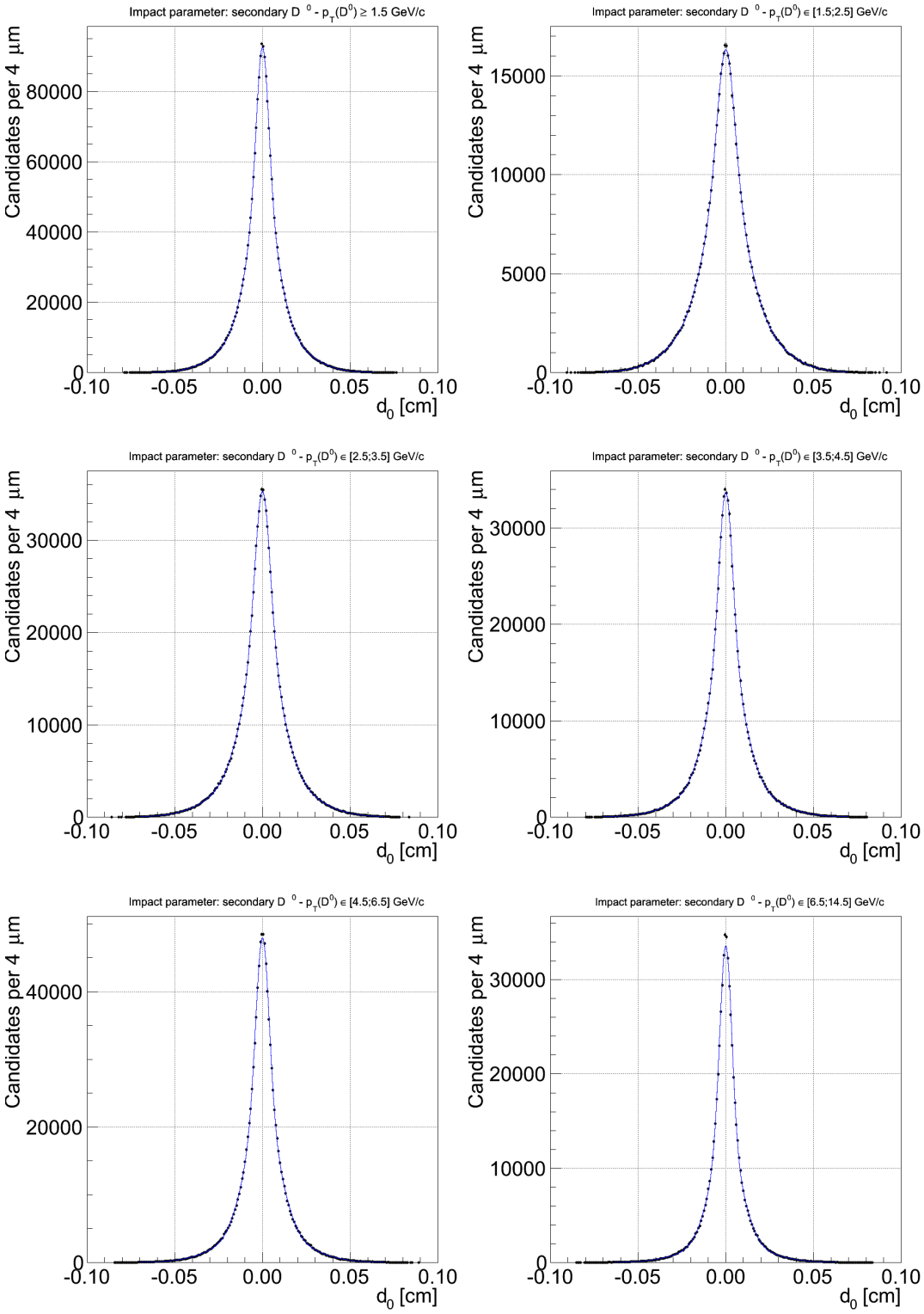

Figure 19: *$d_0(D^0)$ distribution of MC events for the secondary D^0 component for each bin of $p_T(D^0)$ and for $p_T(D^0) \geq 1.5$ GeV/c.*

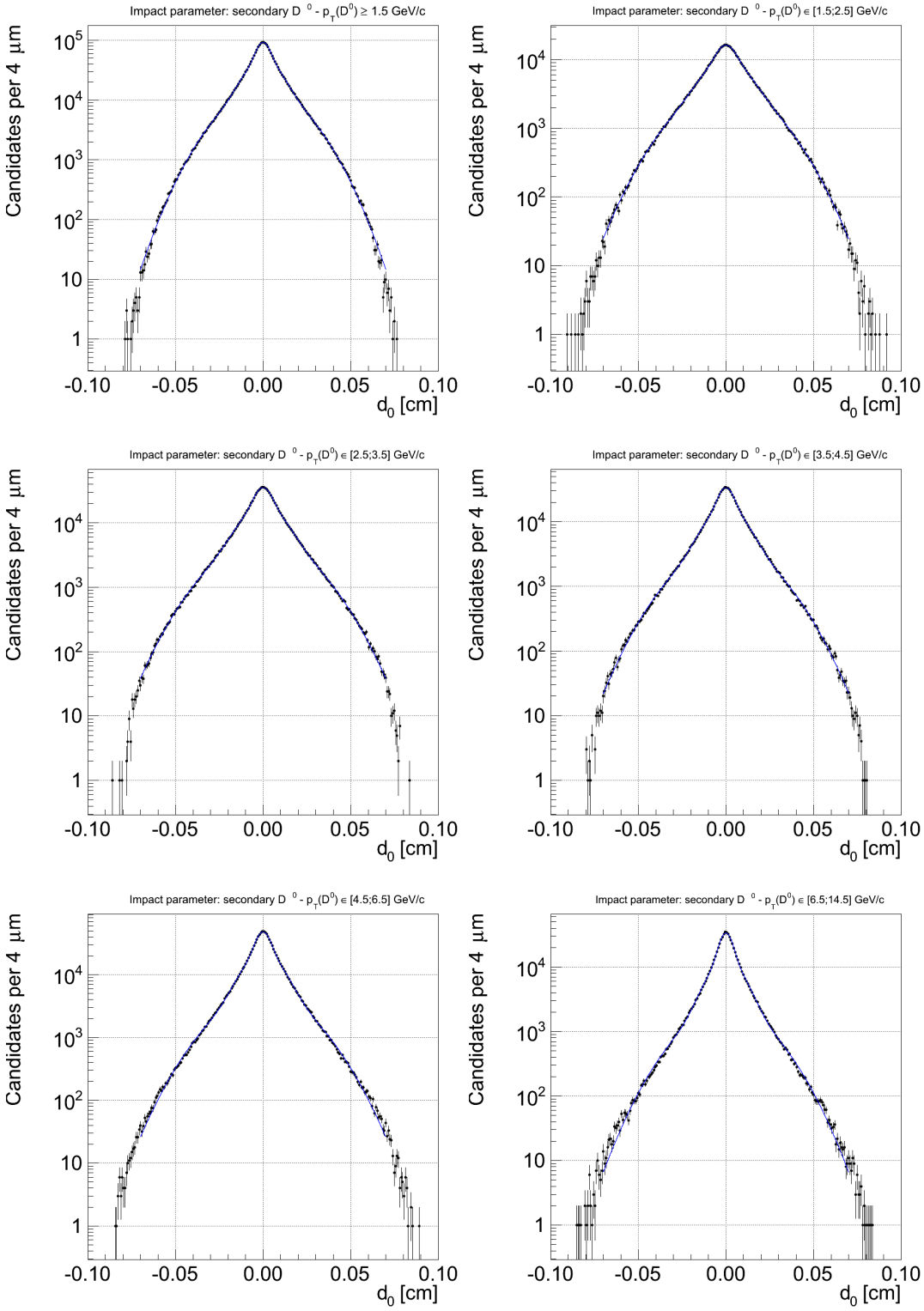

Figure 20: *$d_0(D^0)$ distribution of MC events for the secondary D^0 component for each bin of $p_T(D^0)$ and for $p_T(D^0) \geq 1.5$ GeV/c.*

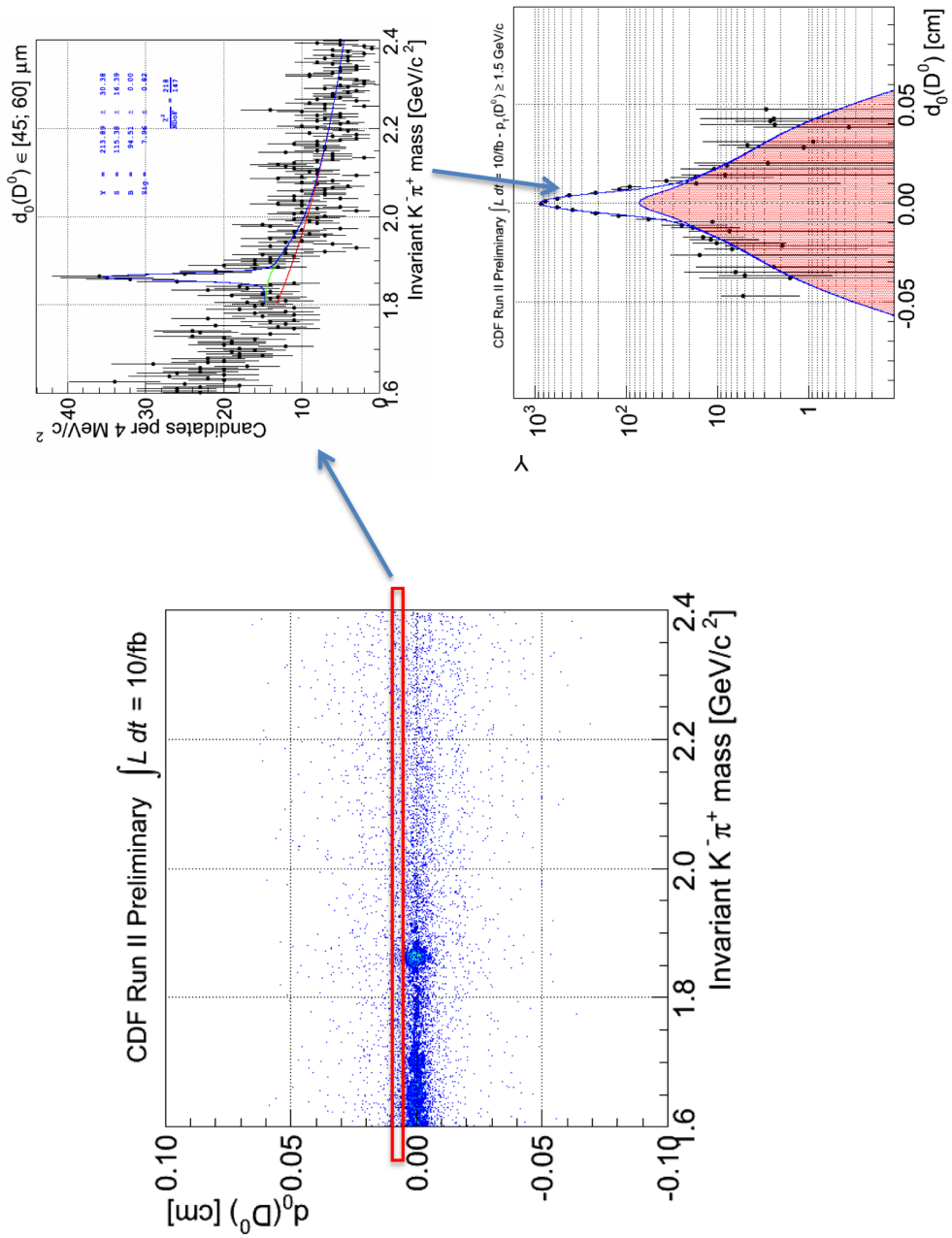

Figure 21: *Visual description of the steps needed to measure the direct fraction of* D^0.

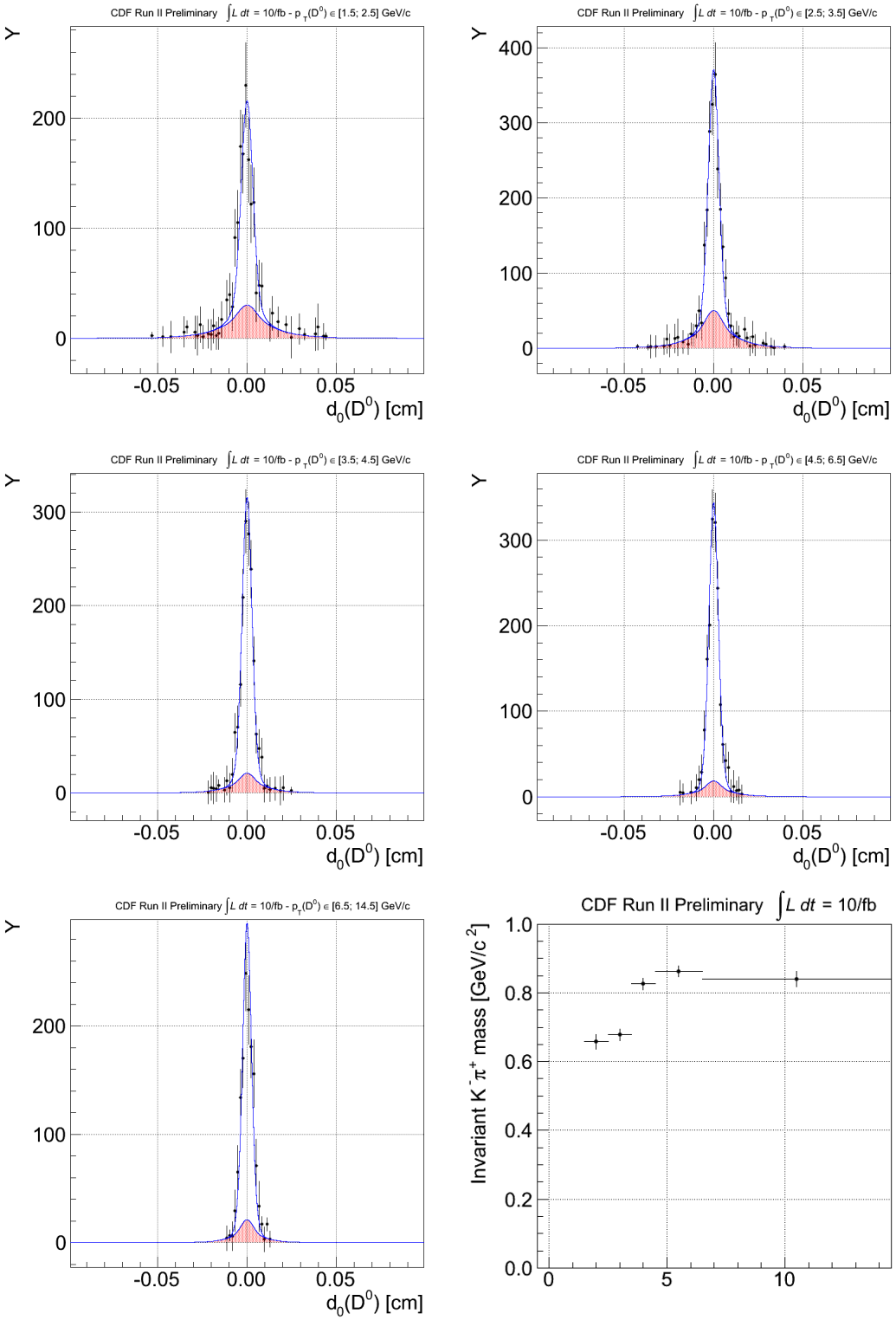

Figure 22: *D^0 direct fraction (f_D) fits as a function of $p_T(D^0)$.*

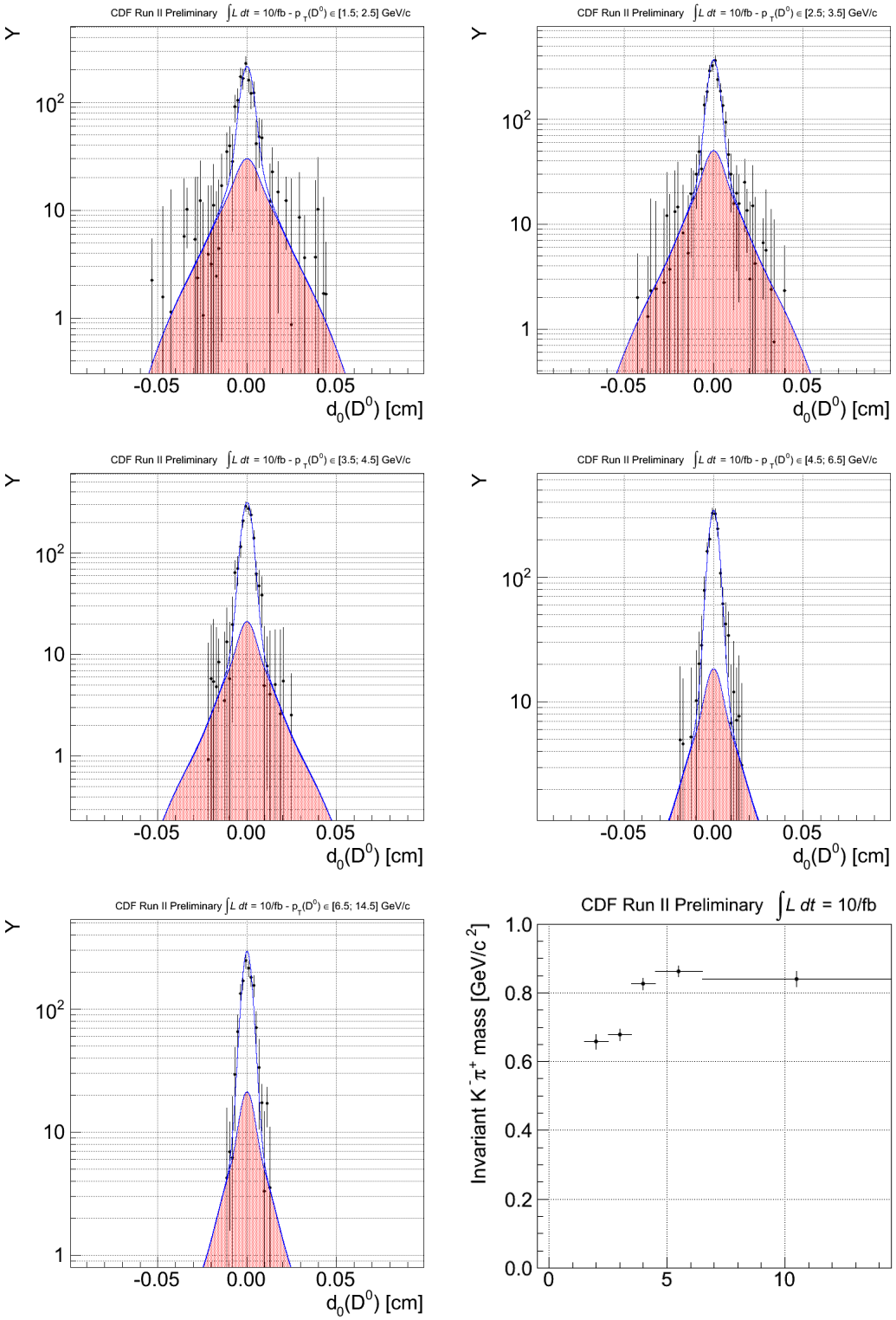

Figure 23: *D^0 direct fraction (f_D) fits as a function of $p_T(D^0)$.*

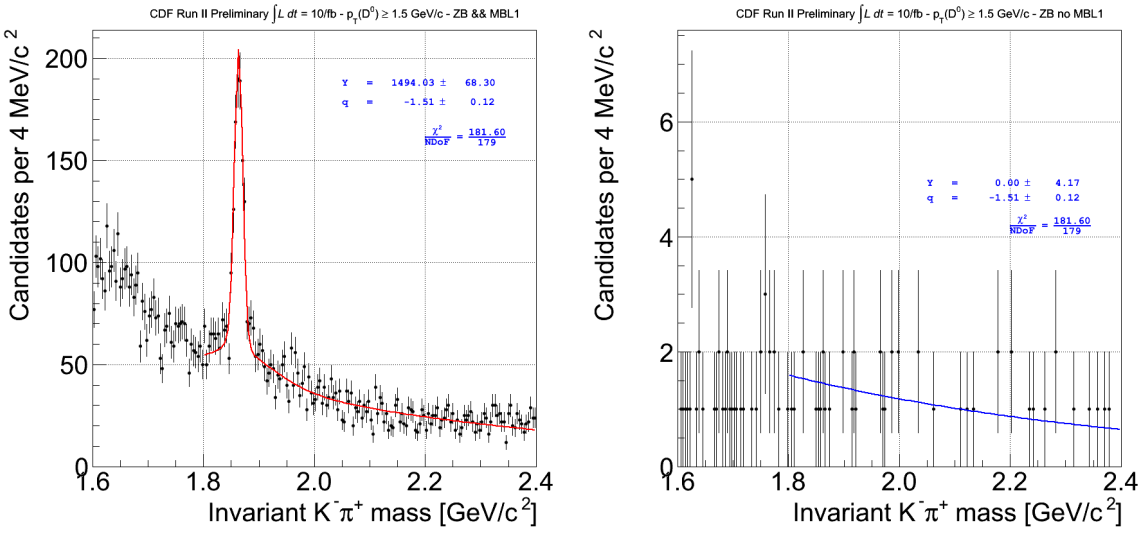

Figure 24: *Result of the combined fit of the invariant $K^-\pi^+$ mass plots for candidates of ZB events that fired (left) or not (right) the MB trigger.*

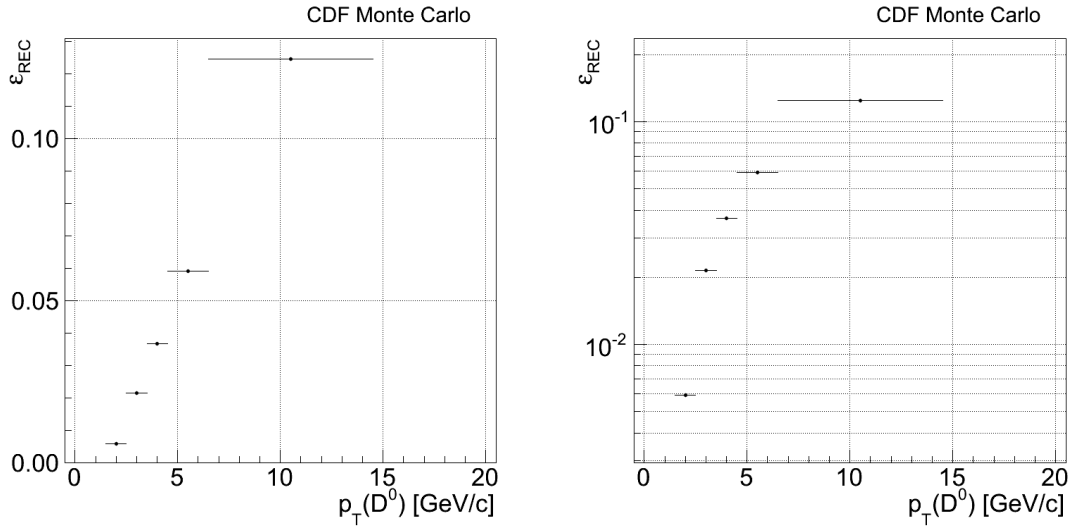

Figure 25: *Reconstruction efficiency as a function of $p_T(D^0)$: linear (left) and log (right) scale.*

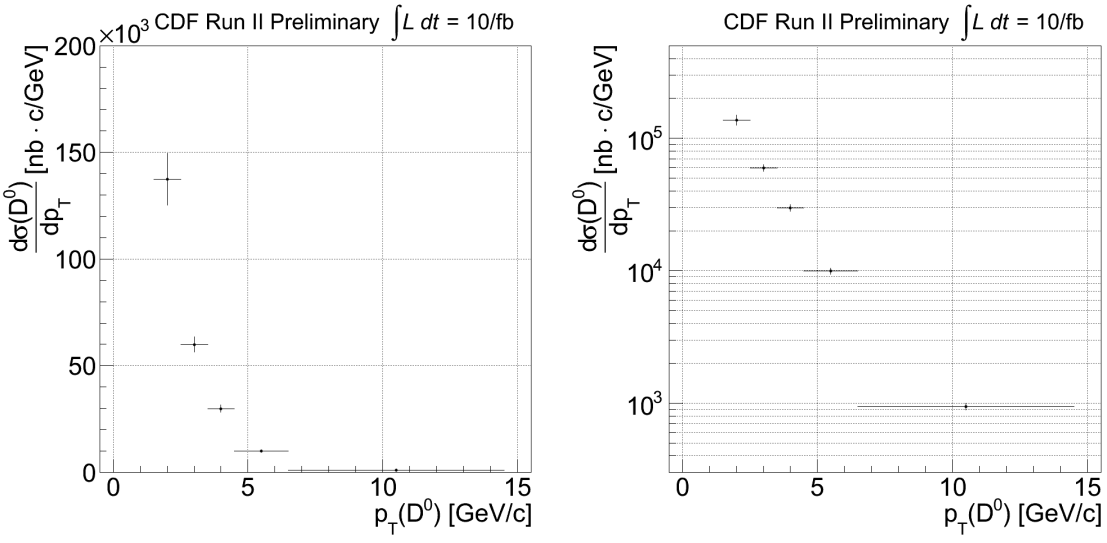

Figure 26: *Measured D^0 production cross section as a function of $p_T(D^0)$: linear (left) and log (right) scale.*

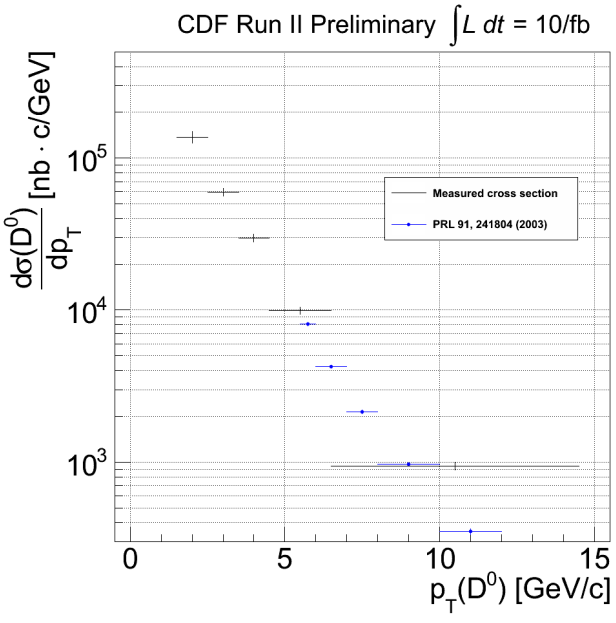

Figure 27: *Measured (black) and CDF published (blue) D^0 production cross section as a function of $p_T(D^0)$.*

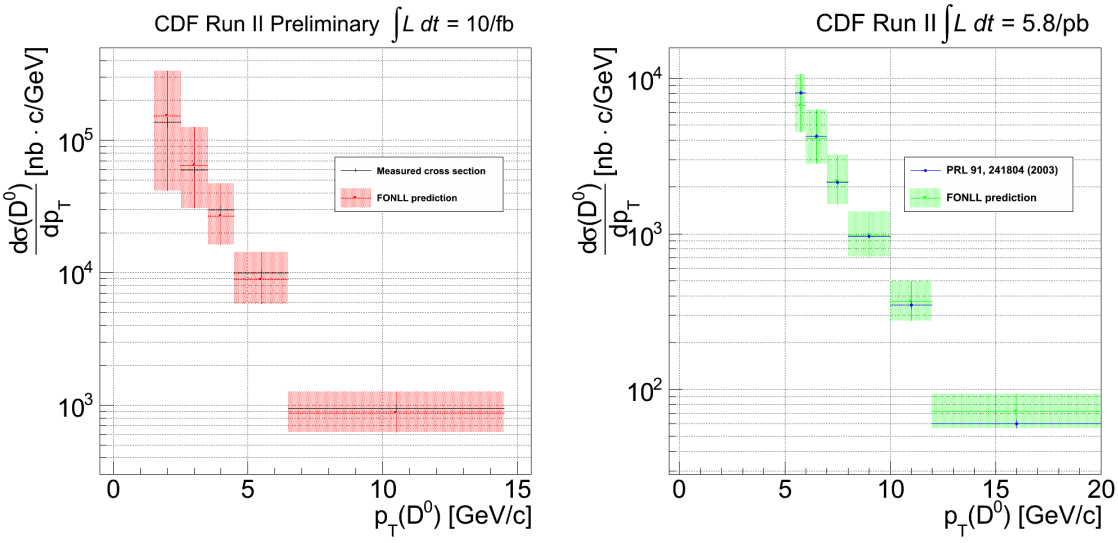

Figure 28: *Measured (left) and CDF published (right) D^0 production cross section as a function of $p_T(D^0)$ compared to FONLL prediction.*

References

[1] D. Acosta *et al.* [CDF Collaboration], Phys. Rev. Lett. **91**, 241804 (2003).

[2] Chunhui Chen, Rolf Oldeman and Joseph Kroll, CDF Note 6177.

[3] M. Cacciari, S. Frixione, M. L. Mangano, P. Nason and G. Ridolfi, "QCD analysis of first b cross section data at 1.96-TeV," JHEP **0407** (2004) 033.

[4] Niccolò Moggi, Michael Joseph Morello, Manuel Mussini, Giovanni Punzi, Franco Rimondi and Diego Tonelli, CDF Note 10079.

[5] S. Jindariani *et al.*, CDF Note 7446.

[6] D. Acosta *et al.*, Phys. Rev. D **50**, 5518 (1994).

[7] S.Klimenko and J.Konigsberg, CDF Note 6314.

[8] J. Peter Berge, CDF Note 7537.

[9] A. Di Canto, G. Punzi, L. Ristori, M.J. Morello and D. Tonelli, CDF Note 10214.

[10] D. Tonelli, CDF Note 9509.

[11] Jonathan Lewis, private communication.

[12] D. Acosta, S. Klimenko, J. Konigsberg, A. Madorsky, A. Nomerotski, A. Sukhanov, D. Tsybychev and S.M. Wang, CDF Note 5861.

[13] D. Acosta, R. Field, S. Klimenko, J. Konigsberg, G. Lungu, V. Necula, A. Pronko, A. Sukhanov, D. Tsybychev and S.M. Wang, CDF Note 6054.

[14] N. Moggi and F. Rimondi, CDF Note 8594.

[15] A. Di Canto, M.J. Morello, G. Punzi, L. Ristori, D. Tonelli, CDF Note 10214.